PRIMARY AMIDE RAMAN VIBRATIONS AS ENVIRONMENTAL AND STRUCTURAL MARKERS OF GLUTAMINE AND ASAPARGINE PROTEIN SIDE CHAINS

by

Elizabeth M. Dahlburg

B.A. in Physics, Kenyon College, 2012

Submitted to the Graduate Faculty of

the Dietrich School of Arts & Sciences in partial fulfillment

of the requirements for the degree of

Master of Science

University of Pittsburgh

2016

UNIVERSITY OF PITTSBURGH

DIETRICH SCHOOL OF ARTS & SCIENCES

This thesis was presented

by

Elizabeth M. Dahlburg

It was defended on

March 3, 2016

and approved by

Sanford A. Asher, Distinguished Professor, Department of Chemistry

Jeffry Madura, Professor, Department of Chemistry and Biochemistry, Duquesne University

Seth Horne, Associate Professor, Department of Chemistry

Thesis Advisor: Sanford A. Asher, Distinguished Professor, Department of Chemistry

PRIMARY AMIDE RAMAN VIBRATIONS AS ENVIRONMENTAL AND STRUCTURAL MARKERS OF GLUTAMINE AND ASAPARGINE PROTEIN SIDE CHAINS

Elizabeth M. Dahlburg, M.S.

University of Pittsburgh, 2016

UV resonance Raman (UVRR) is a powerful spectroscopic technique for the study of protein conformation and dynamics. Excitation at ∼200 nm selectively enhances secondary amide vibrations, which are sensitive to the peptide backbone secondary structure and local environment. Primary amide bands are also resonance enhanced in UVRR spectra and could be used to report on glutamine and asparagine side chains in biophysical studies of proteins and peptides.

IR absorption, visible Raman, and UVRR were used to investigate the small primary amide molecule propanamide. Dramatic spectral changes in the primary amide vibrations were observed upon aqueous solvation. Aqueous solvation impacts the dielectric and hydrogen bonding environment of the primary amide group resonance structures. This leads to a decrease in C–O and increase in C–N bond order of the primary amide group and therefore alters the resonance enhancement and vibrational frequencies of the primary amide vibrations substantially. Due to this significant response, several primary amide bands can be used as sensitive environmental markers for the glutamine and asparagine side chains.

Visible Raman and UVRR spectra of L-glutamine and five derivative molecules, D-glutamine, N-Acetyl-L-glutamine, L-glutamine t-butyl ester, Glycyl-L-glutamine, and L-seryl-L-asparagine, were collected and assigned in the 950-1200 cm^{-1} region. The OCCC dihedral angle of each was determined from X-ray crystal structures. An empirical relationship between the $AmIII^{P}$ vibrational frequency and the OCCC dihedral angle was observed.

This dependence can be explained by hyperconjugation that occurs between the C_β–C_γ σ orbital and the C=O π^* orbital of the primary amide group. This interaction induces an increase in the C_β–C_γ bond length. As the C_β–C_γ bond length increases, the stretching force constant decreases, downshifting the $AmIII^P$ band. Due to this sensitivity, the $AmIII^P$ can be used as a structural marker diagnostic of the OCCC dihedral angle, such as in the side chains glutamine and asparagine in peptide and protein conformational studies.

TABLE OF CONTENTS

LIST OF TABLES

LIST OF FIGURES

1.0 INTRODUCTION

1.1 MOTIVATION FOR NEW BIOPHYSICAL TOOLS

Polyglutamine expansion in proteins and aggregation into polyglutamine-rich fibril-like aggregates in neuronal cells is associated with several neurodegenerative diseases, including Huntington's disease and several spinocerebellar ataxias [1–8]. In order to understand the molecular origins of these diseases, the biophysical properties of simple polyglutamine peptides have been a subject of intense study.

Fibril aggregation studies have revealed mechanisms of fibril nucleation and growth [9–14]. Models of fibrils structures have been proposed based on X-ray diffraction [15–17] and solid-state NMR (ssNMR) [14, 18–21], but there is as yet no consensus and, until very recently, little was known about the structures of the glutamine side chains. Two distinct populations of glutamine side chains have been observed in fibrils by ssNMR [14, 19, 20, 22]. Sharma et al. interpret X-ray fiber diffraction data to reveal the glutamine side chains in a uncommon bent conformation [17]. Peptide microcrystal studies suggest that the tendency to form fibril polymorphs could possibly be due to side chain interactions [23]. Van der Wel and coworkers observe interdigitated extended side chains in the core of huntingtin exon 1 fibrils using ssNMR [22]. Glutamine side chains are believed to play an important role in the structure and aggregation mechanisms of polyglutamine peptides and could be important for formation or stabilization of fibrils [11, 15, 16, 19, 22, 24].

UV resonance Raman (UVRR) spectroscopy can provide molecular-level insights into protein structures such as polyglutamine fibrils that are insoluble and cannot be crystallized. Primary amide bands are resonance enhanced in UVRR spectra [25] and could act as spectral markers for glutamine side chains. These bands could be used as new spectroscopic tools to

investigate the local environments and structures of glutamine side chains in polyglutamine studies.

1.2 RAMAN SPECTROSCOPY

The Raman Effect. Raman scattering is an inelastic light scattering phenomenon in which a molecule is excited and radiates energy at frequencies different from the incident radiation. The differences in energy correspond to the nuclear vibrational motions of the molecule which couple with the electron cloud oscillations created by the incident radiation [26–28]. Raman spectroscopy measures the intensity of the inelastically scattered light and the frequency shifts that occur. This differs from Infrared (IR) spectroscopy, which measures the absorption of different frequencies of light and depends on net changes in the dipole moment as the molecule vibrates. Both vibrational spectroscopies are used to measure molecular vibrations of a sample in order to study the molecular structure, dynamics, and environment.

UV Resonance Raman Spectroscopy (UVRR). When excitation occurs within an electronic absorption band of a molecule or specific chromophore in a sample, large enhancement of the scattering intensity is observed for certain vibrations. The enhanced vibrations are those that couple with driven electronic motion in the electronic transition. This is called resonance Raman because the excitation frequency is in resonance with the electronic transition. Figure 1 shows IR absorption, Raman scattering, and resonance Raman scattering.

Biophysical Applications of UVRR. UVRR is an excellent technique for the study of proteins conformation and dynamics [29]. The selective enhancement of particular vibrations that are diagnostic of dielectric environment, hydrogen bonding, and structure enables the study of complicated molecules such as proteins in solution and in the solid-state. Excitation at ∼200 nm selectively enhances secondary amide vibrations [30], which have been shown to depend on hydrogen bonding [31–34] and peptide backbone secondary structure. Asher and coworkers determined a powerful quantitative relationship between the Amide III_3 vibration and Ramachandran Ψ angle [35–38]. This relationship can be used to calculate Ψ angle distributions and determine the Gibbs free energy landscape along the Ψ angle coordinate.

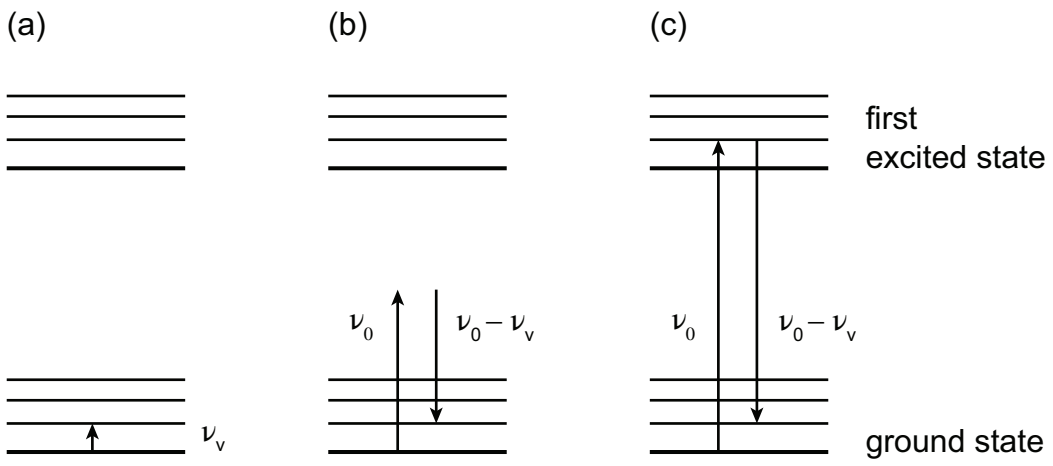

Figure 1: Energy level diagrams of (a) IR absorption (b) Raman scattering (c) resonance Raman scattering.

These studies have made possible remarkable investigations of protein and peptide structure and folding [25, 39–44].

In addition, UVRR can be used to investigate the structure, and hydrogen bonding, and local environment of protein side chains. For example, the hydrogen bonding environment of aromatic amino acids can be determined based on UV resonance Raman cross sections [45]. Takeuchi and coworkers developed an empirical relationship between the W3 band of tryptophan and the $\chi^{2,1}$ torsion angle [46–48]. Hong et al. [49] found that the hydration state of the side chain arginine is related to the Raman cross section and frequency. Histidine specific vibrations were found to be sensitive to protonation state [50, 51]. A proline tertiary amide vibration, also resonance enhanced near ∼200 nm, shows sensitivity to peptide conformation [52–54]. The deep understanding of the relationships between these bands and the structural and environmental characteristics of the backbone and side chains allows for incisive studies of proteins and peptides.

2.0 PRIMARY AMIDE VIBRATION AQUEOUS SOLVATION DEPENDENCE

2.1 INTRODUCTION

The primary amide group is present in the protein side chains glutamine and asparagine. These side chains are of particular interest because of their ability to hydrogen bond with the protein backbone and other side chains, and their presence in disease proteins with elongated polyglutamine segments [1–8] and prions [55]. Primary amide bands are resonance enhanced in UV resonance Raman spectra [25] due the first $\pi \rightarrow \pi^*$ (NV_1) transition of the primary amide group and could be used to report on these side chains in biophysical studies of proteins and peptides. Raman and Infrared (IR) spectra were collected of the small molecule propanamide because it is a model of the glutamine and asparagine side chains. A full assignment was completed and large spectral changes were observed upon aqueous solvation. Several bands act as sensitive spectroscopic markers diagnostic of the environment of the primary amide group. These spectral markers will be of use in studies of glutamine and asparagine side chains in peptides and proteins.

2.2 MATERIALS AND METHODOLOGY

2.2.1 Sample Preparation

Propanamide ($CH_3CH_2CONH_2$, 97% purity) was purchased from Acros Organics and used as a solid sample without further purification. The N-deuterated crystalline sample was

obtained by multiple rounds of recrystallization in D_2O (99.9% atom D purity), obtained from Cambridge Isotope Laboratories, Inc.

Solutions of propanamide in H_2O and D_2O were prepared at 30 mM concentrations. In mixtures of acetonitrile (HPLC, far-UV grade), purchased from Acros Organics, and H_2O, 30 mM propanamide concentrations were used. As an internal standard, sodium perchlorate ($NaClO_4$, ≥98% purity), purchased from Sigma-Aldrich, was used at 200 mM concentration. N-methylacetamide ($CH_3CH_2CONHCH_3$, NMA, ≥99% purity) was purchased from Sigma-Aldrich and prepared at 10 mM concentration in H_2O.

2.2.2 Infrared Spectroscopy

IR spectroscopy was performed on a PerkinElmer Spectrum 100 FTIR with a Universal ATR accessory (UATR). Propanamide crystals were lightly ground with a mortar and pestle for ∼30 s, placed on the diamond crystal, and subjected to ∼145 N of applied force with the pressure arm. The spectrum was measured in the mid-infrared from 600–4000 cm^{-1} with 1 cm^{-1} resolution.

2.2.3 Visible Raman Spectroscopy

Visible Raman spectra were collected on a Renishaw inVia Raman microscope with 633 nm excitation generated by a HeNe laser. Spectra were collected at 2 cm^{-1} resolution from 100–4000 cm^{-1} using a 5× objective lens. The following acetonitrile bands were used for calibration [56]: 380 cm^{-1}, 918 cm^{-1}, 1376 cm^{-1}, 2249 cm^{-1}, and 2942 cm^{-1}.

2.2.4 UV Resonance Raman Spectroscopy

229 nm excitation. UV resonance Raman (UVRR) spectra of crystalline samples were measured using cw 229 nm excitation of a Coherent Innova 300c FreD frequency doubled Ar^+ laser [57]. The Raman scattered light was collected and dispersed using a SPEX Triplemate spectrometer that has been adapted for use in the UV. The dispersed light was then detected with a Spec-10 system CCD camera (Princeton Instruments, Model 735-0001) with

Lumagen-E coating. Solid samples were spun on a brass spinning cell to prevent thermal- and photodegredation. The 380 cm^{-1}, 918 cm^{-1}, 1376 cm^{-1}, 2249 cm^{-1}, and 2942 cm^{-1} bands of acetonitrile were used for calibration.

204 nm excitation. UVRR spectra of solution samples were measured using 204 nm excitation. The 204 nm light was obtained by Raman shifting the third harmonic of a Coherent Infinity Nd:YAG laser with H_2 gas at ∼30 psi and selecting the fifth anti-Stokes line. Scattered Raman light was collected and dispersed with double monochromator adapted for use in the UV with a subtractive configuration. The light was then imaged on a Spec-10 CCD. Solution samples were circulated through a temperature-controlled (20 °C) flow-cell to prevent photodegredation products contributing to spectra.

2.2.5 UV Absorption Spectroscopy

UV absorption spectra were collected on a Varian Cary 500 spectrophotometer using a 0.2 mm path length quartz cuvette (Hellma Analytics).

2.3 RESULTS AND DISCUSSION

2.3.1 Vibrational Assignment of Propanamide

In order to complete a full assignment of the vibrational spectrum of propanamide (Figure 2), IR, visible Raman, and pre-resonance 229 nm excitation Raman spectra of solid-state samples and 204 nm excitation resonance Raman spectra of propanamide in solution were collected. These experimental results were interpreted with normal mode analysis completed using new density functional theory DFT calculations. DFT calculations and normal mode analysis were performed by Dr. Zhenmin Hong and Dr. Nataliya S. Myshakina, and analyzed with David Punihaole, as described in detail in [58].

Crystalline Propanamide. Figures 3 and 4 show IR, visible Raman, and 229 nm excitation UVRR spectra of crystalline propanamide. To assist in band assignments, spectra of N-deuterated propanamide, $CH_3CH_2CODH_2$, shown in Figures 5 and 6 were collected [58].

At 229 nm excitation, the UVRR spectra are pre-resonance enhanced, since the excitation wavelength falls within the first $\pi \rightarrow \pi^*$ (NV_1) electronic transition absorption band of the primary amide group, at ∼180 nm. The geometry is expected to expand along the C–N coordinate within this transition from the ground electronic state to the first excited electronic state [30, 59]. Therefore, bands with significant C–N stretching character are expected to be resonance enhanced.

The IR and visible Raman vibrational frequencies, DFT scaled, calculated frequencies, and vibrational potential energy distributions are listed in Tables 1 and 2. Figure 2 shows the optimized geometry of propanamide, with labels corresponding the potential energy distribution (PED) analysis.

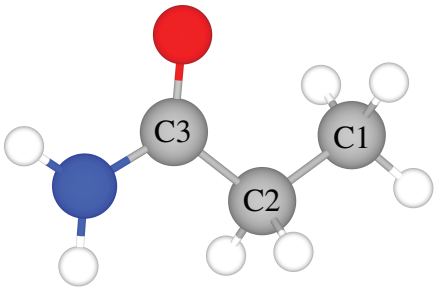

Figure 2: Propanamide molecule with numbering scheme used in potential energy distributions. Adapted with permission from [58]. Copyright © 2015, American Chemical Society.

2000–3500 Wavenumber Region. The 2000–3500 cm^{-1} region is made up of C–H and N–H stretching vibrations. The N–H stretching bands are identified by the significant downshift they undergo upon N-deuteration. The N–H asymmetric stretch is located at ∼3355 cm^{-1} and the symmetric stretch at ∼3175 cm^{-1}. The bands between 2700 and 3100 cm^{-1} do not shift upon N-deuteration, indicating that they are all C–H stretching vibrations.

Note that there are two bands in this region of the spectrum that are not assigned to fundamentals. The band at ∼2735 cm^{-1} is not shifted in the spectrum of N-deuterated propanamide. Further, Kuroda et al. [60] show that this vibration does not shift upon

deuteration of the methylene group. This demonstrates that the vibration is not due to an overtone or combination of either the amide or the methylene group. Thus, the ∼2735 cm^{-1} band is assigned to an overtone of the ∼1380 cm^{-1} CH_3 symmetric deformation. The band at ∼2940 cm^{-1} is also not shifted in the spectrum of N-deuterated propanamide, but is very strong in the visible Raman and UVRR spectra. This band is assigned to a Fermi resonance between the CH_3 stretching mode and the ∼1460 cm^{-1} CH_3 asymmetric deformation. This assignment is based on the work of Kuroda et al. [60] and Nolin and Jones [61] and contests the assignment of Nandini and Sathyanarayana [62]. This band frequency is higher than the typical seen for a CH_2 stretching vibration [63], which Nandini and Sathyanarayana suggested [62].

1500–1800 Wavenumber Region. This region contains more complex vibrations made up of heavy atom stretching and bending motions, especially involving the amide group. The ∼1675 cm^{-1} band is assigned to the Amide I (AmI) vibration, made up of ∼75% C=O stretching with ∼7% C–N stretching according to the calculations. The Amide II (AmII) band at ∼1590 cm^{-1} band is made up of ∼86% NH_2 scissoring with a small C–N stretching contribution of ∼10%. These bands are both well defined in the visible Raman and UVRR spectra, but broad and overlapping in the IR spectrum. This is most likely due to the presence of phonons and differences in phonon selection rules between the two phenomena.

The shifts in vibrational frequencies observed upon N-deuteration support the assignment and PED analysis of the AmI and AmII vibrations. The AmI band downshifts from ∼1675 cm^{-1} to ∼1610 cm^{-1} in the Raman spectra, indicating that the AmI vibration is mostly C=O stretching. In the N-deuterated spectrum, there is no AmII band, rather a band appears at ∼1170 cm^{-1} which is attributed to ND_2 scissoring. This supports the idea that the AmII vibration is mostly NH_2 scissoring.

1200–1500 Wavenumber Region. Between 1200 and 1500 cm^{-1} there are several bands made up of CH_3 and CH_2 deformation and bending motions. The vibrations at ∼1464 cm^{-1} and ∼1450 cm^{-1} are assigned to CH_3 asymmetric deformations. At ∼1380 cm^{-1} is the CH_3 symmetric deformation. The CH_2 twisting mode is assigned to the band at ∼1260 cm^{-1}.

Within this region there are also bands that contain significant C–N stretching character. Previously, Kuroda et al. [60] and Nandini and Sathyanarayana [62] assigned the vibration at

$\sim$1420 cm^{-1} to a CH_2 scissoring/C–N stretching mode and a CH_2 bending/CH_3 symmetric bending mode, respectively. Nandini and Sathyanarayana [62] assign the $\sim$1300 cm^{-1} band to a vibration made up of C–N stretching/CH_2 wagging while Kuroda et al. [60] assign it to mostly CH_2 wagging.

The UVRR spectra collected show a resonance enhanced band at $\sim$1430 cm^{-1}, which is not resolved in the visible Raman or IR spectra. This analysis suggests that this band be assigned to a complex vibration, ν_{12}, made up of $\sim$30% CH_2 wagging, $\sim$20% C–C stretching, and $\sim$19% C–N stretching. The $\sim$1420 cm^{-1} band is assigned to CH_2 wagging and the $\sim$1300 cm^{-1} band to another complex vibration, ν_{15}, which contains CH_2 wagging and C–N stretching.

700–1200 Wavenumber Region. The 700–1200 cm^{-1} region contains vibrations made up of NH_2 rocking, CH_2 rocking, CH_3 rocking, and C–CH_3 stretching. The band at $\sim$1145 cm^{-1} is assigned to NH_2 rocking since it downshifts to $\sim$940 cm^{-1} upon N-deuteration. The band at $\sim$1070 cm^{-1} is assigned to ν_{19}, a vibration made of $\sim$38% C–CH_3 stretching, significant $\sim$29% NH_2 rocking, and $\sim$16% C–N stretching character, which differs from the normal mode analysis of Kuroda et al. [60].

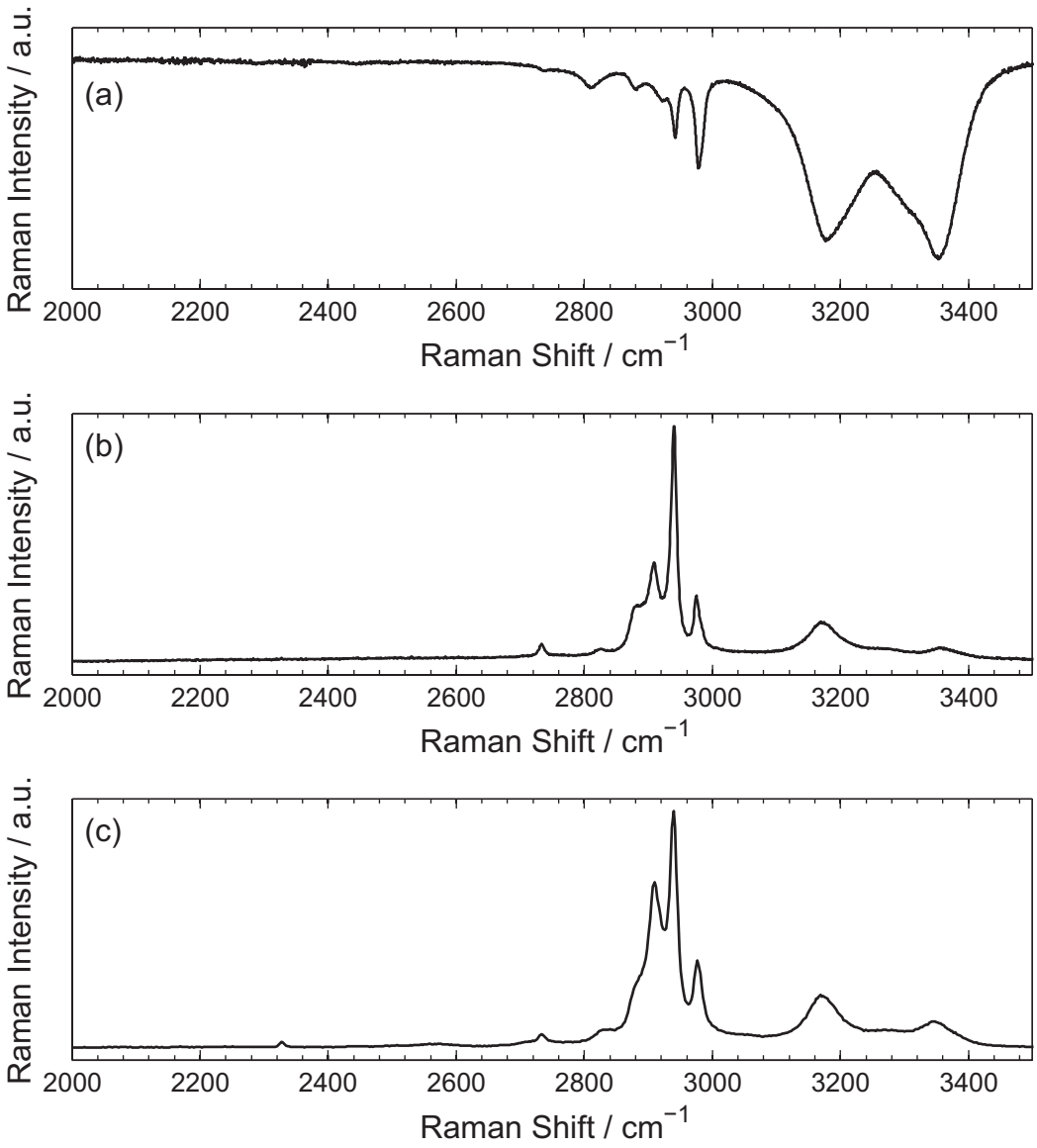

Figure 3: (a) IR (b) visible Raman, and (c) UVRR spectra of crystalline propanamide in the 2000–3500 cm^{-1} region.

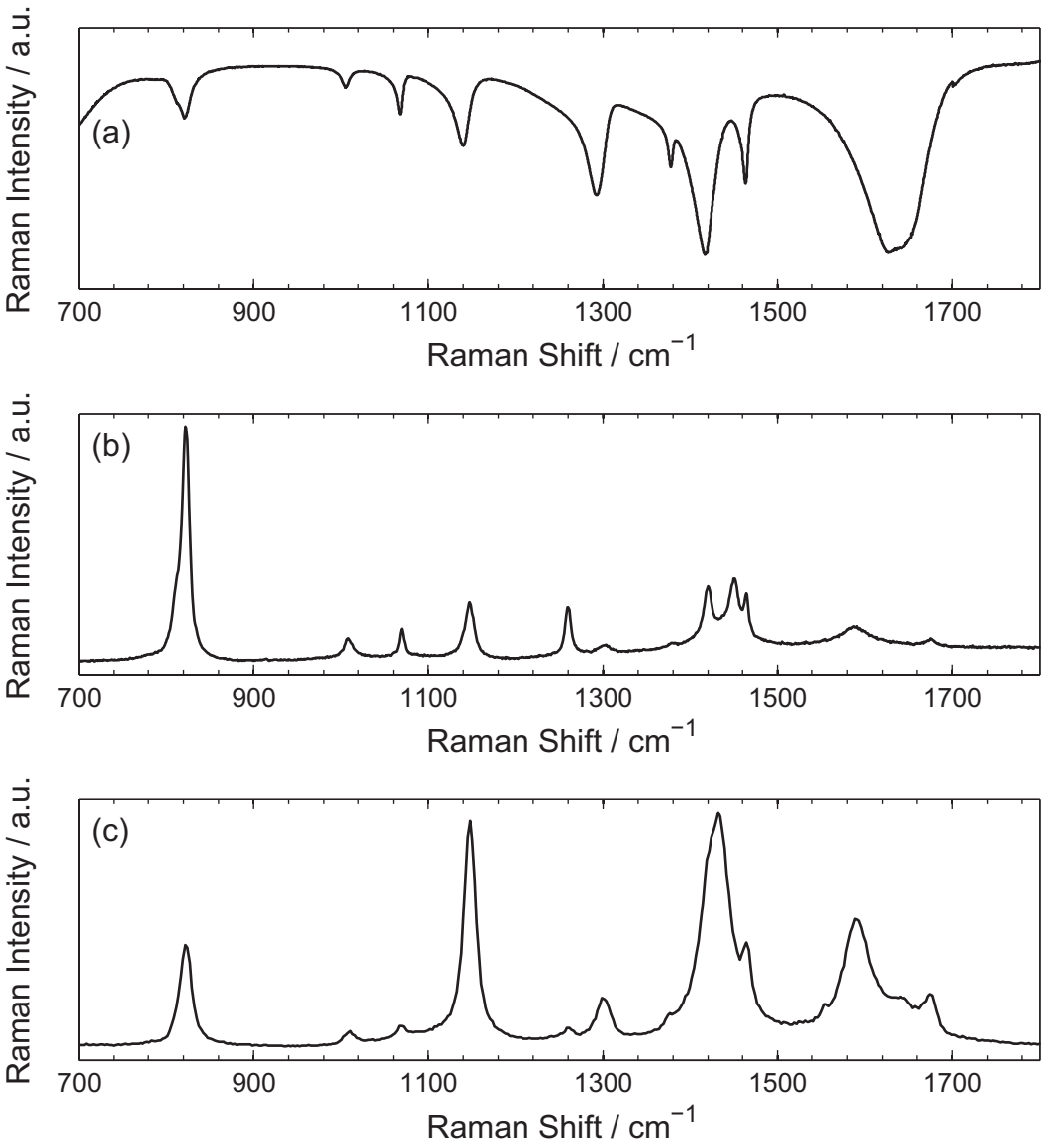

Figure 4: (a) IR (b) visible Raman, and (c) UVRR spectra of crystalline propanamide in the 700–1800 cm^{-1} region.

Table 1: Assignments of IR and Raman Bands of Crystalline Propanamide

	Infrared[a]	Raman[a]	Calc.	Δ^b (%)	PED[c] (≥5% contribution)
ν_1	3356	3356	3434	2.3	νNH (57), $-\nu$NH (43)
ν_2	3177	3171	3319	4.6	νNH (57), νNH (43)
ν_3	2979	2975	2906	2.4	νC1H (69), $-\nu$C1H (22)
ν_4	2979	2975	2894	2.8	νC1H (49), $-\nu$C1H (45)
$2\nu_{10}$	2943	2940	–		–
ν_5	2922	2909	2866	1.7	νC2H (75), $-\nu$C2H (19)
ν_6	2882	2882	2830	1.8	νC1H (42), νC1H (32), νC2H (23)
ν_7	2811	2827	2825	0.2	νC2H (76), νC2H (20)
$2\nu_{14}$	2737	2734	–		–
ν_8	1643	1676	1667	0.5	νC=O (75), $-\nu$CN (7), δ_sNC(O)C (7)
ν_9	1628	1588	1562	2.9	σNH_2 (86), νCN (10)
ν_{10}	1464	1464	1453	0.7	$\delta'_{as}CH_3$ (43), $-\delta_{as}CH_3$ (38), $\rho'CH_3$ (8)
ν_{11}	–	1450	1443	0.5	$\delta_{as}CH_3$ (51), δ_{as}'CH_3 (39), $-\rho'CH_3$ (8)
ν_{12}	–	1430[d]	1393	2.6	ωCH_2 (30), νC2C3 (20), $-\nu$CN (19), $-\beta$C=O (10), $-\nu$C1C2 (7), $\delta'_{as}CH_3$ (6)
ν_{13}	1418	1420	1422	0.2	σCH_2 (89)
ν_{14}	1379	1381	1374	0.4	$\delta_s CH_3$ (89), νC1C2 (6)
ν_{15}	1294	1302	1278	1.6	ωCH_2 (31), νCN (28), $-\tau CH_2$ (12), βC=O (8), ρNH_2 (5)
ν_{16}	–	1260	1271	0.9	τCH_2 (61), ωCH_2 (13), $-\rho'CH_3$ (7), $-\rho CH_2$ (6)
ν_{17}	1141	1148	1130	1.3	ρNH_2 (30), $-\nu$C1C2 (19), $\rho'CH_3$ (11), $-\rho CH_3$ (10), $-\nu$C=O (8), δ_sNC(O)C (7), δCCC (7)
ν_{18}	1068	1070	1108	3.6	ρCH_2 (27), $-\rho CH_3$ (21), $-\tau CH_2$ (17), $-\rho'CH_3$ (16), $-\Pi$C=O (11)
ν_{19}	1068	1070	1090	1.9	νC1C2 (38), ρNH_2 (26), $-\nu$CN (16), ρCH_3 (6)
ν_{20}	1007	1009	1028	2.0	$\rho'CH_3$ (28), ωCH_2 (19), νC1C2 (18), $-\rho CH_3$ (11), $-\nu$C2C3 (9), $-\rho CH_2$ (8)
ν_{21}	822	822	853	3.8	ρCH_2 (23), $\rho'CH_3$ (18), $-\Pi$C=O (18), ρCH_3 (15), τCH_2 (10), νC2C3 (8)
ν_{22}	811	812	850	4.7	νC2C3 (43), $-\rho CH_3$ (14), ρNH_2 (11), $-\rho CH_2$ (7), νC1C2 (6)

[a] Infrared and Raman vibrational frequencies reported in wavenumbers (cm^{-1})

[b] $\Delta = |\nu_{obs} - \nu_{calc}|/\nu_{obs} \times 100$ %

[c] ν: stretch; δ_s: sym deformation; σ: scissoring; δ_{as}: asym deformation; ρ: rocking; ω: wagging; β: in-plane bending; τ: twisting; Π: out-of-plane bending

[d] Frequency obtained from 229 nm excitation UVRR data.

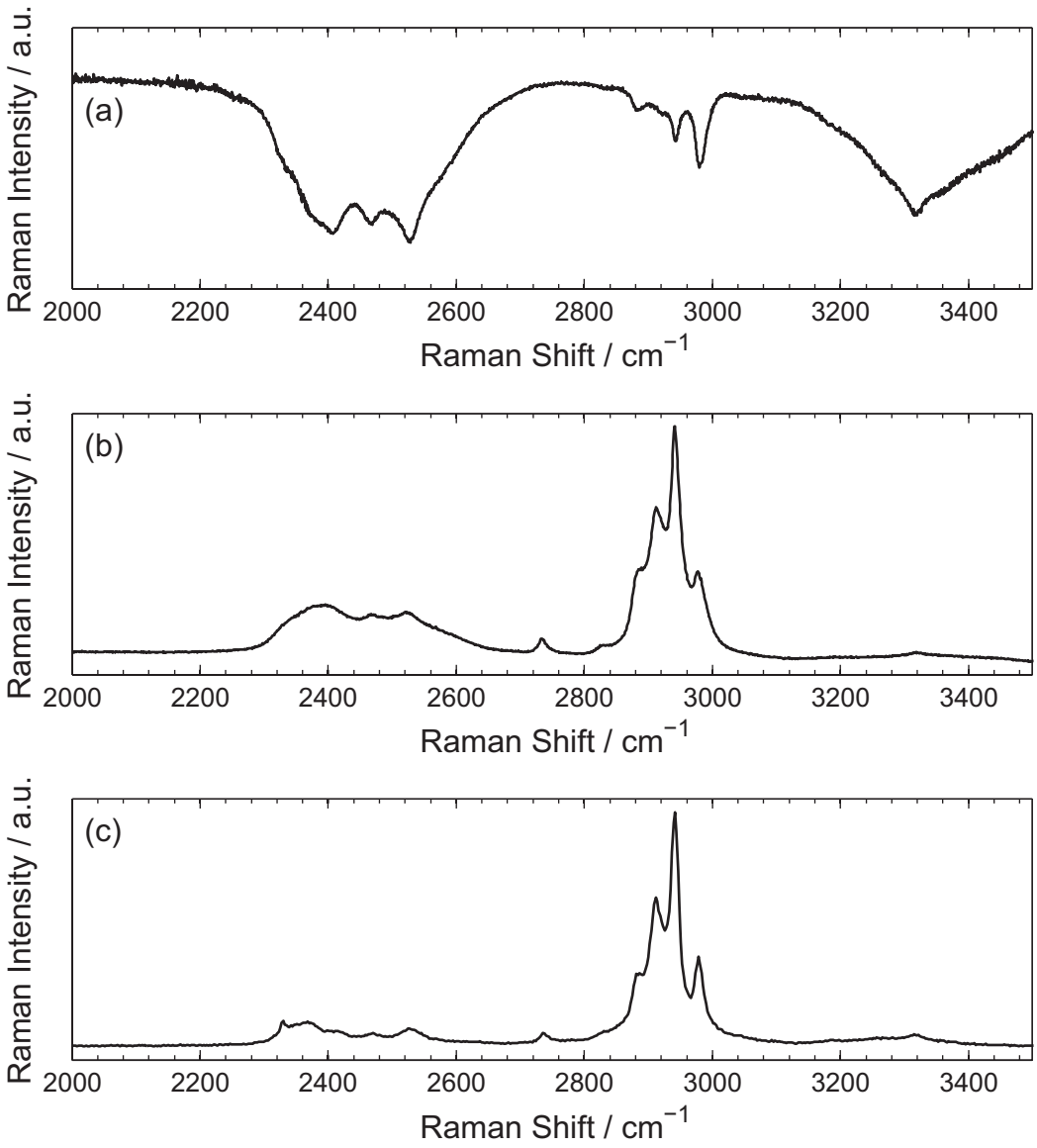

Figure 5: (a) IR (b) visible Raman, and (c) UVRR spectra of crystalline N-deuterated propanamide in the 2000–3500 cm^{-1} region.

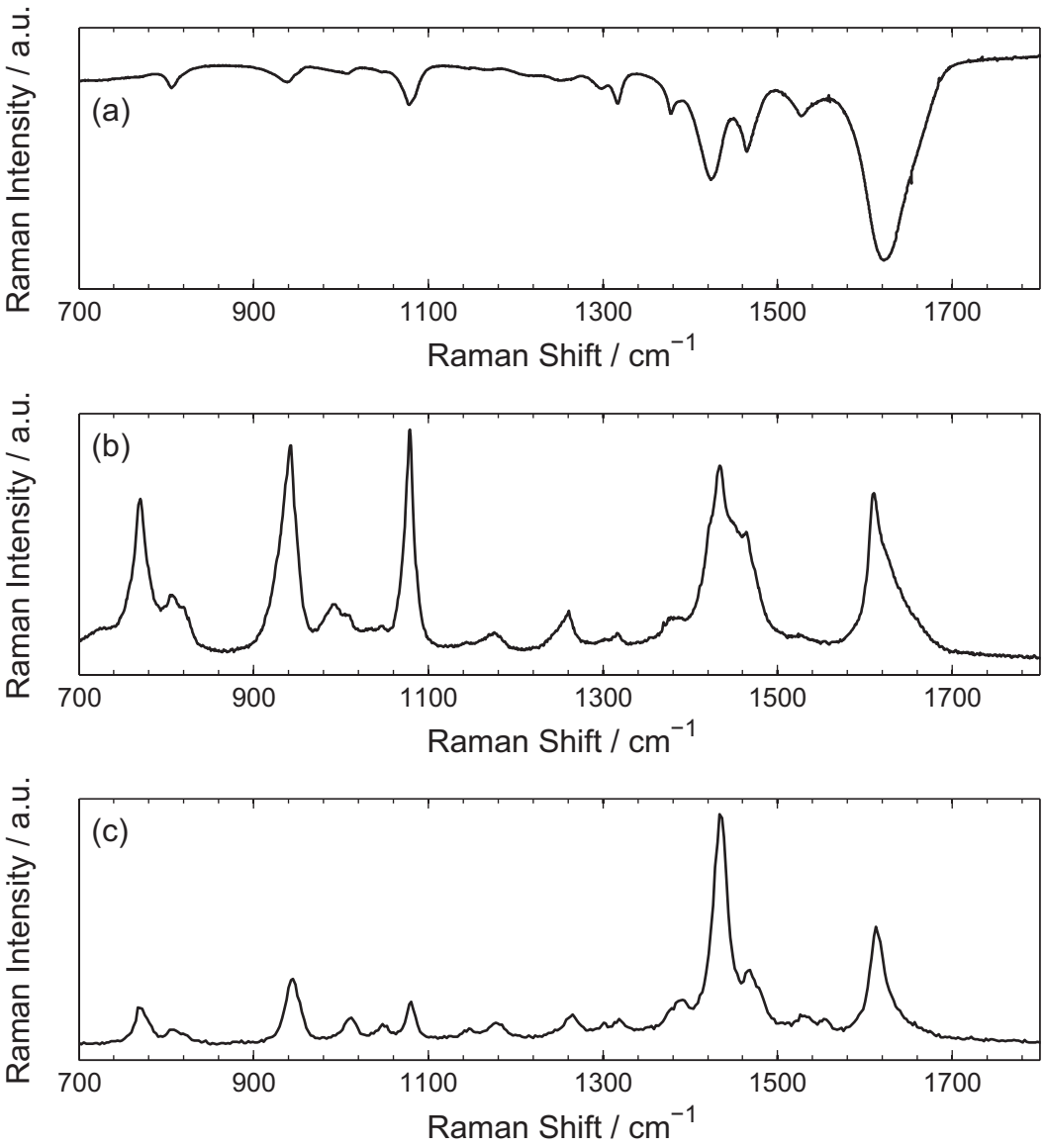

Figure 6: (a) IR (b) visible Raman, and (c) UVRR spectra of crystalline N-deuterated propanamide in the 700–1800 cm^{-1} region.

Table 2: Assignments of IR and Raman Bands of Deuterated Crystalline Propanamide

	Infrared[a]	Raman[a]	Calc.	Δ^b (%)	PED[c] (≥5% contribution)
ν_1	2981	2977	2941	1.3	νC1H (69), $-\nu$C1H (22)
ν_2	2981	2977	2929	1.7	νC1H (49), $-\nu$C1H (45)
$2\nu_{10}$	2943	2941	–	–	–
ν_3	2923	2912	2900	0.6	νC2H (75), $-\nu$C2H (19)
ν_4	2884	2886	2863	0.8	νC1H (42), νC1H (32), νC1H (23)
ν_5	–	2833	2858	0.9	νC2H (76), νC2H (20)
$2\nu_{13}$	–	2734	–	–	–
ν_6	2527	2523	2607	3.3	νND (54), $-\nu$ND (45)
ν_7	2407	2393	2458	2.4	νND (54), νND (45)
ν_8	1623	1610	1662	2.8	νC=O (78), δ_sNC(O)C (7), $-\nu$CN (7)
ν_9	1466	1464	1447	1.2	δ'_{as}CH$_3$ (42), $-\delta_{as}$CH$_3$ (37), ρ'CH$_3$ (8)
ν_{10}	–	1450	1437	0.9	δ_{as}CH$_3$ (52), δ'_{as}CH$_3$ (38), -ρCH$_3$ (8)
ν_{11}	–	1434[d]	1401	2.3	νCN (33), $-\omega$CH$_2$ (19), $-\nu$C2C3 (19), βC=O (10), $-\delta'_{as}$CH$_3$ (6), δ_sND$_2$ (5)
ν_{12}	1425	1422	1415	0.6	σCH$_2$ (89)
ν_{13}	1379	1378	1367	0.8	δ_sCH$_3$ (89), νC1C2 (8)
ν_{14}	1318	1317	1295	1.7	ωCH$_2$ (45), νCN (23), δ_sND$_2$ (15),
ν_{15}	–	1261	1261	0.0	τCH$_2$ (75), -ρCH$_3$ (9), -ρ'CH$_3$ (5)
ν_{16}	1168	1176	1134	3.2	δ_sND$_2$ (60), βC=O (12), νC2C3 (8), $-\omega$CH$_2$ (5)
ν_{17}	1079	1079	1093	1.3	νC1C2 (35), ρCH$_3$ (19), $-\rho'$CH$_3$ (11), $-\delta$CCC (7), $-\delta_s$NC(O)C (5)
ν_{18}	1079	1079	1091	1.1	ρCH$_2$ (25), $-\rho'$CH$_3$ (19), ρCH$_3$ (17), $-\tau$CH$_2$ (16), $-\Pi$C=O (11), νC1C2 (7)
ν_{19}	1007	1006	1019	1.2	νC1C2 (33), ρ'CH$_3$ (20), ωCH$_2$ (14), $-\nu$C2C3 str (9), $-\rho$CH$_3$ (6), δ_sND$_2$ (5)
–	989	992	–	–	
ν_{20}	940	942	936	0.5	ρND$_2$ (34), $-\nu$CN (15), $-\rho'$CH$_3$ (11), δ_sNC(O)C (9), δ_sND$_2$ (8) ρCH$_3$ (6)
–	–	819	–	–	–
ν_{21}	807	806	828	2.7	ρCH$_2$ (29), ρCH$_3$ (24), $-\Pi$C=O (19), ρ'CH$_3$ (13), τCH$_2$ (12)
ν_{22}	–	770	776	0.7	νC2C3 (51), ρND$_2$ (25), $-\delta$CCC (7)

[a] Infrared and Raman vibrational frequencies reported in wavenumbers (cm^{-1})

[b] $\Delta = |\nu_{\text{obs}} - \nu_{\text{calc}}|/\nu_{\text{obs}} \times 100$ %

[c] ν: stretch; δ_s: sym deformation; σ: scissoring; δ_{as}: asym deformation; ρ: rocking; ω: wagging; β: in-plane bending; τ: twisting; Π: out-of-plane bending

[d] Frequency obtained from 229 nm excitation UVRR data.

Propanamide in Aqueous Solution. UVRR spectra of propanamide were collected in H_2O and D_2O and shifts were observed in the vibrational frequencies of several bands compared to the crystal spectra [58]. Figure 7(a) shows the AmI band of propanamide in H_2O at $\sim$1669 cm^{-1}, $\sim$7 cm^{-1} downshifted, and the AmII band at $\sim$1610 cm^{-1}, $\sim$22 cm^{-1} upshifted from the spectra of the solid-state sample. The ν_{12} and ν_{19} bands do not shift significantly, but the NH_2 rocking vibration is $\sim$16 cm^{-1} downshifted.

In D_2O (Figure 7(b)), the AmI' upshifts to $\sim$1633 cm^{-1} when compared with crystalline propanamide spectra. The ND_2 scissoring vibration is found at $\sim$1168 cm^{-1}, downshifted from the N-deuterated crystal spectra. The complex vibration, ν_{12}, consisting of $\sim$30% CH_2 wagging, $\sim$20% C–C stretching, and $\sim$19% C–N stretching is found at $\sim$1443 cm^{-1} in D_2O compared to $\sim$1434 cm^{-1} in the spectra of N-deuterated crystalline propanamide.

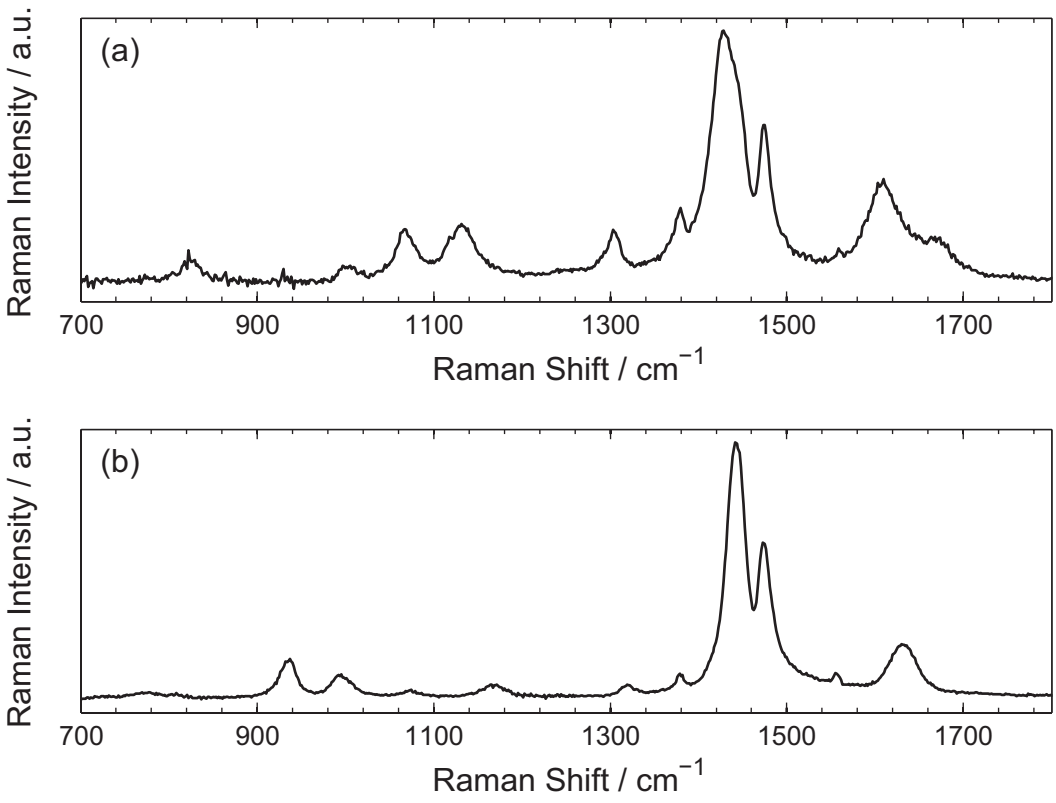

Figure 7: UVRR spectra of propanamide in (a) H_2O and (b) D_2O.

2.3.2 Aqueous Solvation of Primary Amide Vibrations

Upon aqueous solvation, the intensities of UVRR primary amide bands change dramatically [58]. Figure 8 shows large changes in the resonance Raman cross sections and vibrational frequencies of all the bands of propanamide as the solvent transfers from acetonitrile to H_2O. All of the bands show a roughly linear increase in their Raman cross sections as the mole fraction of H_2O increases, except for the AmI band, which shows a decrease in cross section. The AmII and the ν_{12} band show the largest increases.

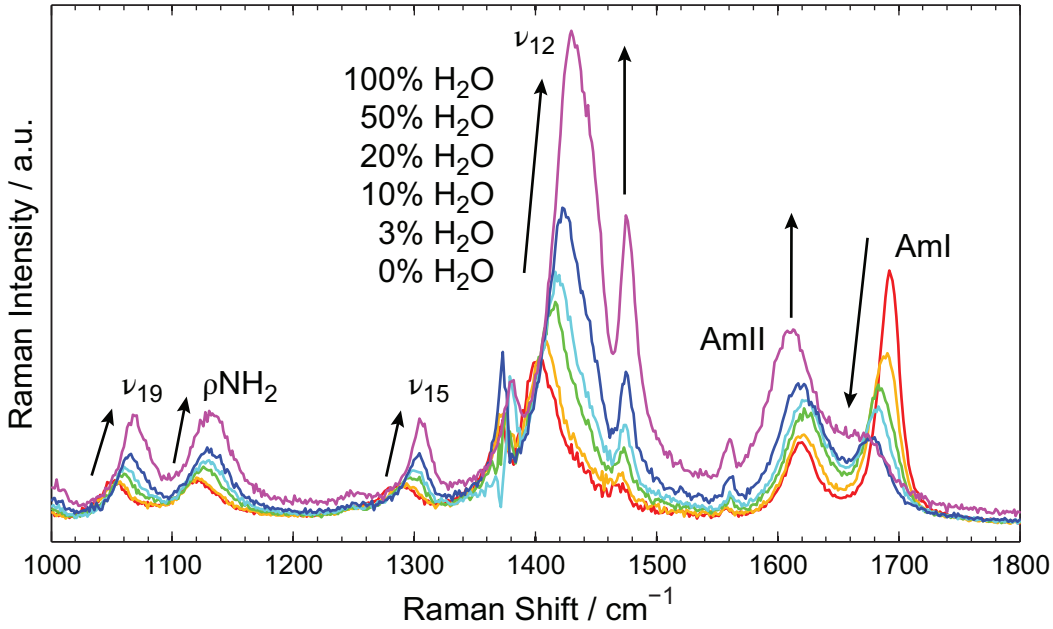

Figure 8: UVRR spectrum of propanamide in mixtures of acetonitrile and H_2O. Adapted with permission from [58]. Copyright © 2015, American Chemical Society.

The vibrational frequencies also show a roughly linear increase in the case of the ν_{12}, NH_2 rocking, and ν_{19} vibrations. In contrast, the AmI and AmII bands show decreases in vibrational frequency as the mole fraction of H_2O increases.

These observations can in part be explained using observations made on other similar amide molecules. The changes in UVRR spectra upon aqueous solvation have previously been noted in valeramide [25] and N-methylacetamide (NMA) [31, 33, 34, 64, 65]. UV absorption

spectra of NMA were collected to compare with those of propanamide (Figure 9) in order to further understand this behavior [58]. Figure 10 shows the UV absorption spectra of NMA in acetonitrile and water. As the mole fraction of water increases, the maximum absorptivity of the NV_1 transition at ∼200 nm, redshifts. Both propanamide and NMA exhibit this redshift in absorptivities, though this is less clear in the case of propanamide for which the NV_1 transition is deeper in the UV (∼ 180 nm). Nielsen and Schellman also observed a redshift of the maximum absorptivity in several primary and secondary amides upon aqueous solvation [66]. It is known that the Raman scattering cross section is proportional to the square of the molar absorptivity. Thus, the changes in the cross sections upon aqueous solvation are due in part to the increase in the molar absorptivity of the NV_1 transition.

However, the dramatic changes in cross sections of the UVRR bands of propanamide are due in larger part to changes in the ground state structure upon aqueous solvation. In the case of secondary amides, the effects of aqueous solvation are attributed to changes in the dielectric and hydrogen bonding on the ground state resonance structures [31, 33, 34, 64, 65]. The dielectric environment and hydrogen bonding of the primary amide group ground state resonance structures are likewise influenced by aqueous solvation.

The primary amide group can act as both a hydrogen bonding donor and as an acceptor with water and itself. The primary amide carbonyl oxygen acts as a hydrogen bonding acceptor while the N–H can act as a hydrogen bonding donor to the oxygen of water. This is possible because water is also both a hydrogen bond acceptor and donor, whereas acetonitrile, being an aprotic polar solvent, can only act as an acceptor. In the case of primary amide group solvated by acetonitrile, the N–H group can act as a hydrogen bonding donor to the nitrogen of acetonitrile, but the carbonyl oxygen is not engaged in hydrogen bonding in this case.

The primary amide group O=C–NH_2 form is more dominant than the $^-$O–C=NH_2^+ resonance structure in a low dielectric and hydrogen bonding environment like acetonitrile. In aqueous solution, where the dielectric constant is higher and hydrogen bonding is stabilizing, the contribution of the dipolar $^-$O–C=NH_2^+ form increases. This is because the partial charges on the carbonyl carbon and nitrogen are expected to increase with hydrogen bonding [67]. The dipolar resonance structure will be less favored when the primary amide

group is solvated by acetonitrile because of the lack of hydrogen bonding with the carbonyl oxygen. Thus, upon aqueous solvation the C–O bond order decreases and the C–N bond order increases in the primary amide group [58, 67].

The decrease in C–O bond order and increase in C–N bond order in amides greatly impacts the Raman cross sections. The resonance Raman cross section scales with the square of the displacement along the enhanced vibration normal coordinate between the electronic ground and electronic excited state geometries [68]. In the case of NMA, vibrations with significant C–N stretching character are resonance enhanced [31, 34, 64, 69, 70] because the molecule is displaced along this normal coordinate between the geometries of the electronic ground and excited states [33, 65, 70]. The AmI of NMA however exhibits less enhancement in water due to the fact that there is less displacement along the C–O normal coordinate.

As the C–O bond order decreases in propanamide, the C–O bond elongates, leading to a decrease in the vibrational frequency of the AmI band, which is mostly C=O stretching. This is because an elongation in the C–O bond corresponds to a decrease in the stretching force constant. The resonance Raman cross section decreases as well because expansion of the electronic excited state along this bond is decreased in water.

As the C–N bond order increases, and thus the C–N bond contracts, vibrations with significant C–N stretching upshift as the stretching force constant increases. The C–N bond order increase also explains the increase in the cross sections. The contraction of the C–N bond leads to an increase in the displacement between the electronic ground and excited state along the C–N coordinate. Thus the vibrations with C–N stretch including the AmII, ν_{12}, ν_{15}, NH_2 rocking, and ν_{19} vibrations are resonance enhanced in the UVRR spectra.

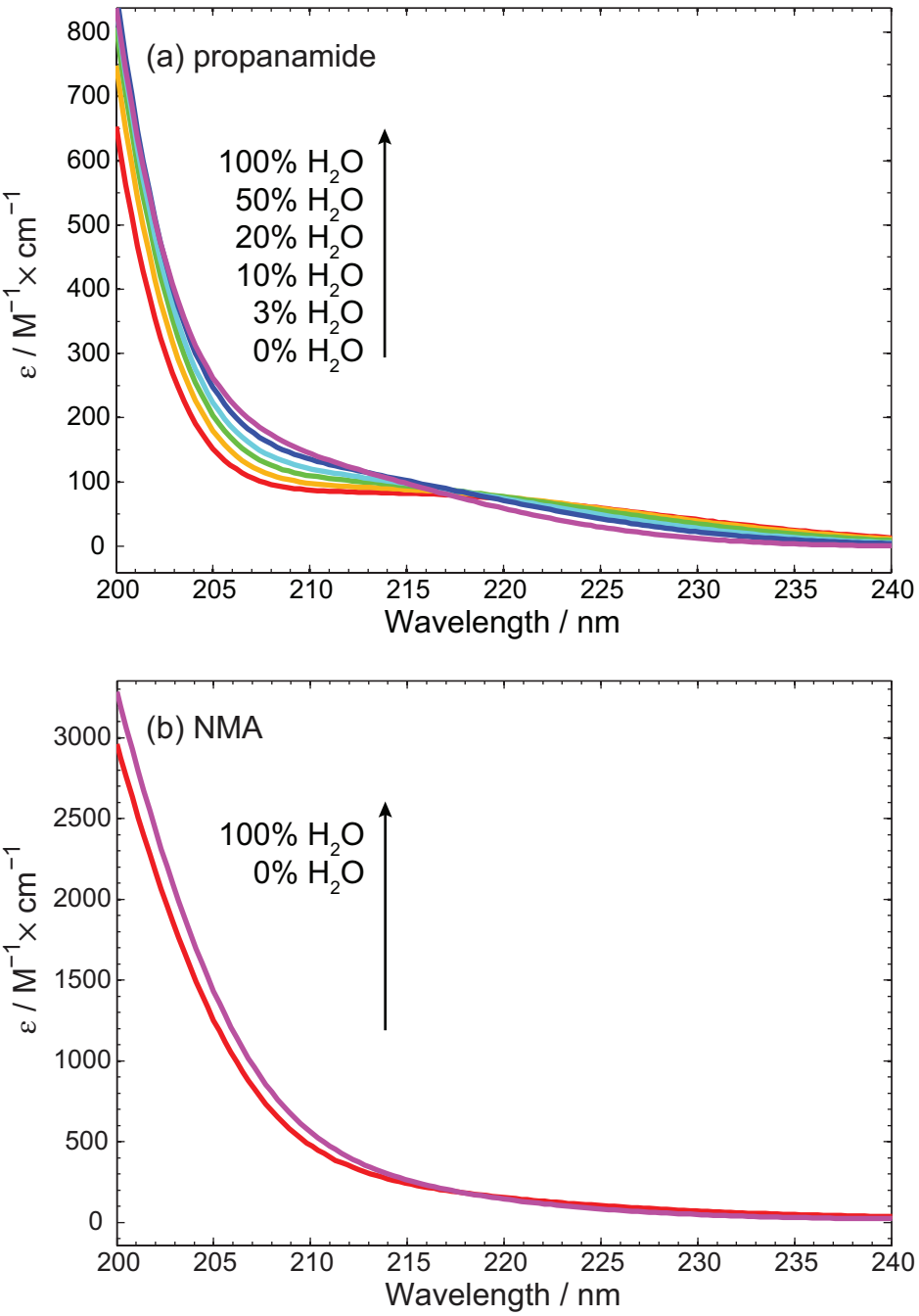

Figure 9: UV Absorption spectrum of (a) propanamide and (b) N-methylacetamide (NMA) in mixtures of acetonitrile and H_2O. Adapted with permission from [58]. Copyright © 2015, American Chemical Society.

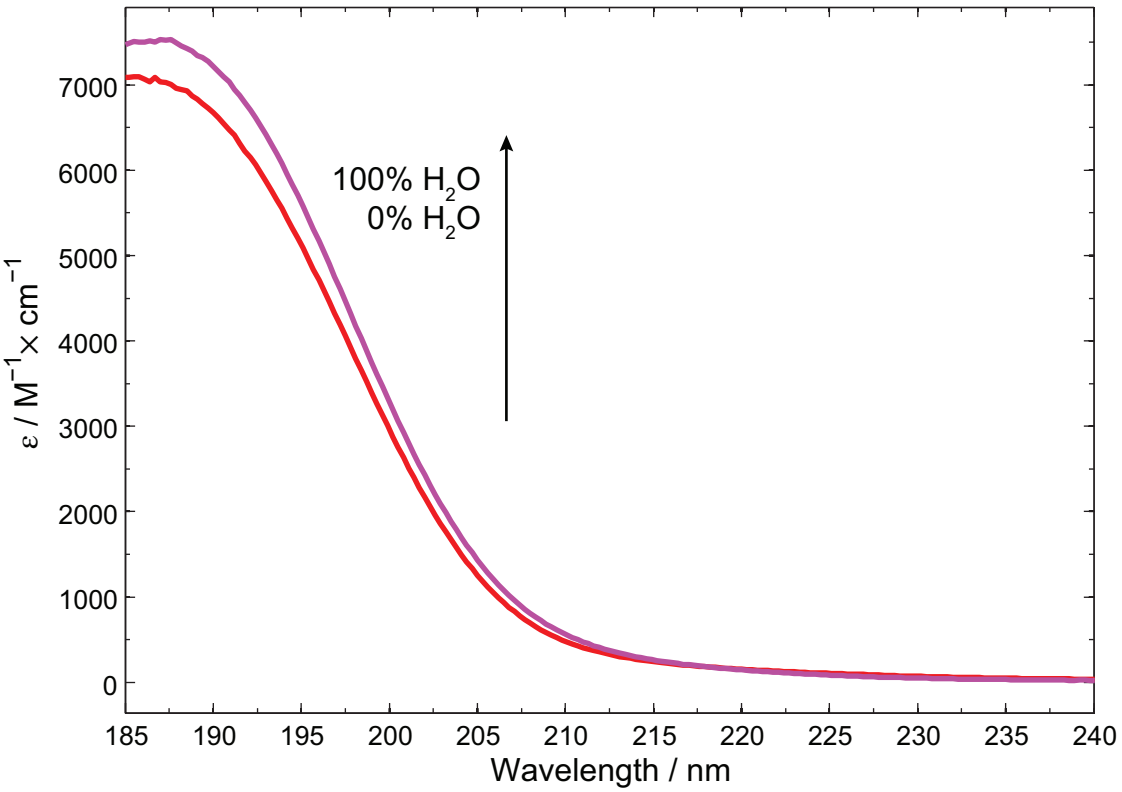

Figure 10: UV Absorption spectrum of NMA in acetonitrile and H_2O from 185 – 240 nm.

3.0 PRIMARY AMIDE VIBRATION STRUCTURAL SENSITIVITY

3.1 INTRODUCTION

Structural markers for glutamine side chains would be of great use in investigations of the aggregation mechanisms of polyglutamine-rich peptides and the structures of the fibril-like aggregates they form. It is not yet well understood how the side chains participate in the aggregation process, though their role appears to be significant [11, 15, 16, 19, 24]. UV resonance Raman (UVRR) spectroscopy has been applied to study the secondary structure and dynamics of proteins in solution using the quantitative relationship between the $AmIII_3$ vibration and the Ramachandran Ψ angle [35–38]. In addition, several side chain vibrations are diagnostic of the local environment [25, 45–47, 49, 53, 71] and in some cases structure [46–48, 52, 54]. Understanding of the structural sensitivity of primary amide vibrations is not as well developed as that of secondary amides. Raman spectra of crystalline L-glutamine and several derivative molecules were collected, and the structures determined by X-ray diffraction. A primary amide Raman band made up of largely NH_2 rocking, C–N stretching, and C–C stretching shows sensitivity to the OCCC dihedral angle. This novel spectroscopic marker will enable the determination of glutamine and asparagine conformations in peptides and proteins.

3.2 MATERIALS AND METHODOLOGY

3.2.1 Sample Preparation

Glycyl-L-glutamine (Gly-Gln, ≥97% purity), purchased from Sigma-Aldrich, and L-seryl-L-asparagine (Ser-Asn, ≥99% purity), purchased from Bachem, were used without further purification. D-glutamine (D-Gln, 98% purity), purchased from Acros Organics, N-Acetyl-L-glutamine (NAcGln, 97% purity), purchased from Spectrum Chemical Mfg. Corp., and L-glutamine t-butyl ester hydrochloride (GlnTBE, ≥98% purity), purchased from Sigma-Aldrich, were all prepared from drying saturated solutions in H_2O (Optima-grade), purchased from Fisher Scientific. L-glutamine (L-Gln, ≥99% purity), purchased from Sigma-Aldrich, was prepared from drying a saturated solution of H_2O with 0.1 M concentration NaCl. N-deuterated crystalline samples were obtained by multiple rounds of recrystallization in D_2O (99.9% atom D purity), obtained from Cambridge Isotope Laboratories, Inc.

3.2.2 Visible Raman Spectroscopy

Visible Raman spectra were collected as described in Section 2.2.3; however, only the 918 cm^{-1}, 1376 cm^{-1} bands of acetonitrile were used for calibration [56].

3.2.3 UV Resonance Raman Spectroscopy

UVRR spectra were collected as described in Section 2.2.4; however, the 801 cm^{-1}, 1028 cm^{-1}, 2852 cm^{-1}, and 2938 cm^{-1} bands of cyclohexane were used to calibrate the 229 nm excitation UVRR spectra.

3.3 RESULTS AND DISCUSSION

3.3.1 Vibrational Assignment of Glutamine and Derivatives

Visible Raman and pre-resonance 229 nm excitation Raman spectra of crystalline L-Gln and five derivative molecules, D-Gln, NAcGln, GLnTBE, Gly-Gln, and Ser-Asn, and 204 nm excitation resonance Raman spectra of L-Gln in solution were collected in order to identify potential spectral markers of conformation of the glutamine side chain. These spectra were assigned in the 950–1200 cm^{-1} region using potential energy distributions obtained from DFT calculations carried out by Dr. Zhenmin Hong and analyzed with David Punihaole, as detailed in [72]. X-ray diffraction of the crystalline samples was performed by David Punihaole and Dr. Steven Geib, described in further detail in [72], providing the molecular structures of the L-Gln and derivative molecule samples (Figures 11 and 12). From these structures, conformational determinants, such as the OCCC dihedral angle, could be obtained.

Crystalline Glutamine and Derivatives. Figures 13, 14, 15, 16, 17, and 18 show the 633 nm visible excitation and 229 nm excitation UVRR spectra of crystalline L-Gln and five derivative molecules: D-Gln, NAcGln, GlnTBE, Gly-Gln, and Ser-Asn. In addition, N-deuterated crystal spectra were collected in order to assist in band assignments, given that the region of interest contains several bands with NH_2 and NH_3 rocking character. As discussed in Section 2.3.1, bands with significant C–N stretching character are expected to exhibit resonance enhancement in 229 nm excitation Raman spectra.

The visible Raman vibrational frequencies, DFT scaled, calculated frequencies, and vibrational potential energy distributions for each molecule in the 950–1200 cm^{-1} region are listed in Tables 3, 4, 5, 6, 7, 8. The crystal structures of L-Gln and derivative molecules with labels corresponding the potential energy distribution analysis and OCCC dihedral angle can be found in Figures 11 and 12.

L-glutamine and D-glutamine. Ramirez and coworkers [73] have reported spectra of solid-state L-glutamine previously [74]; however, they did not use normal mode calculations to complete assignments. New assignments for L-Gln are reported here using UVRR spectral frequencies and intensities, isotopic shifts, and modern DFT calculations. The ex-

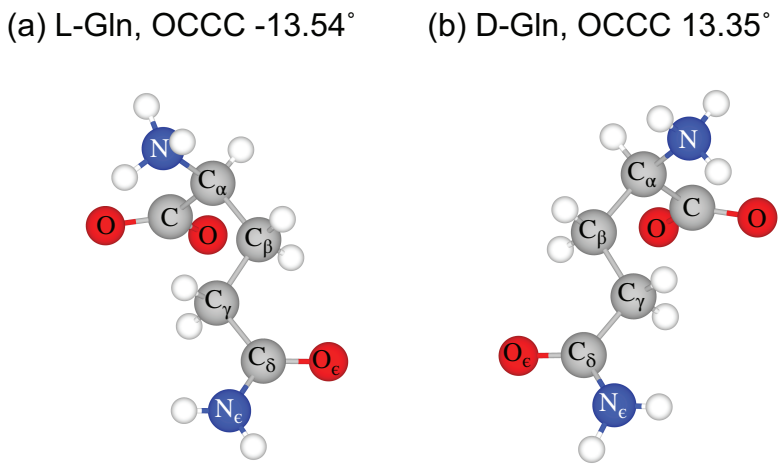

Figure 11: (a) L-glutamine and (b) D-glutamine molecules with labeling scheme used in potential energy distributions. Adapted with permission from [72]. Copyright © 2015, American Chemical Society.

perimentally observed Raman frequencies and assignments of crystalline L-Gln are shown in Table 3 and those of D-Gln in Table 4 and are essentially identical. The ∼1205 cm^{-1} and ∼1166 cm^{-1} bands are assigned to $C_\beta H_2$ twisting/C_α–C_β stretching and C_α–H rocking/$C_\gamma H_2$ twisting modes respectively, as they do not shift in the spectra of N-deuterated L-glutamine. In contrast, the bands at ∼1135 cm^{-1} and ∼1105 cm^{-1} are significantly shifted upon N-deuteration. The ∼1135 cm^{-1} band is assigned to C_β–C_γ stretching/$N_\epsilon H_2$ rocking and the ∼1105 cm^{-1} is assigned to NH_3 rocking. The ∼1079 cm^{-1} band shifts in the N-deuterated spectra as well and is assigned to a band made up of $N_\epsilon H_2$ rocking, out-of-phase C_β–C_γ stretching, and a significant in-phase C_δ–N_ϵ stretching contribution, called the $AmIII^P$ due to its similarity to the secondary Amide III vibration. The ∼1086 cm^{-1}, ∼1052 cm^{-1}, and ∼1000 cm^{-1} bands are composed of mostly C_α–N stretching, NH_3 rocking/C_α–N stretching, and NH_3 rocking/C_α–C_β stretching respectively.

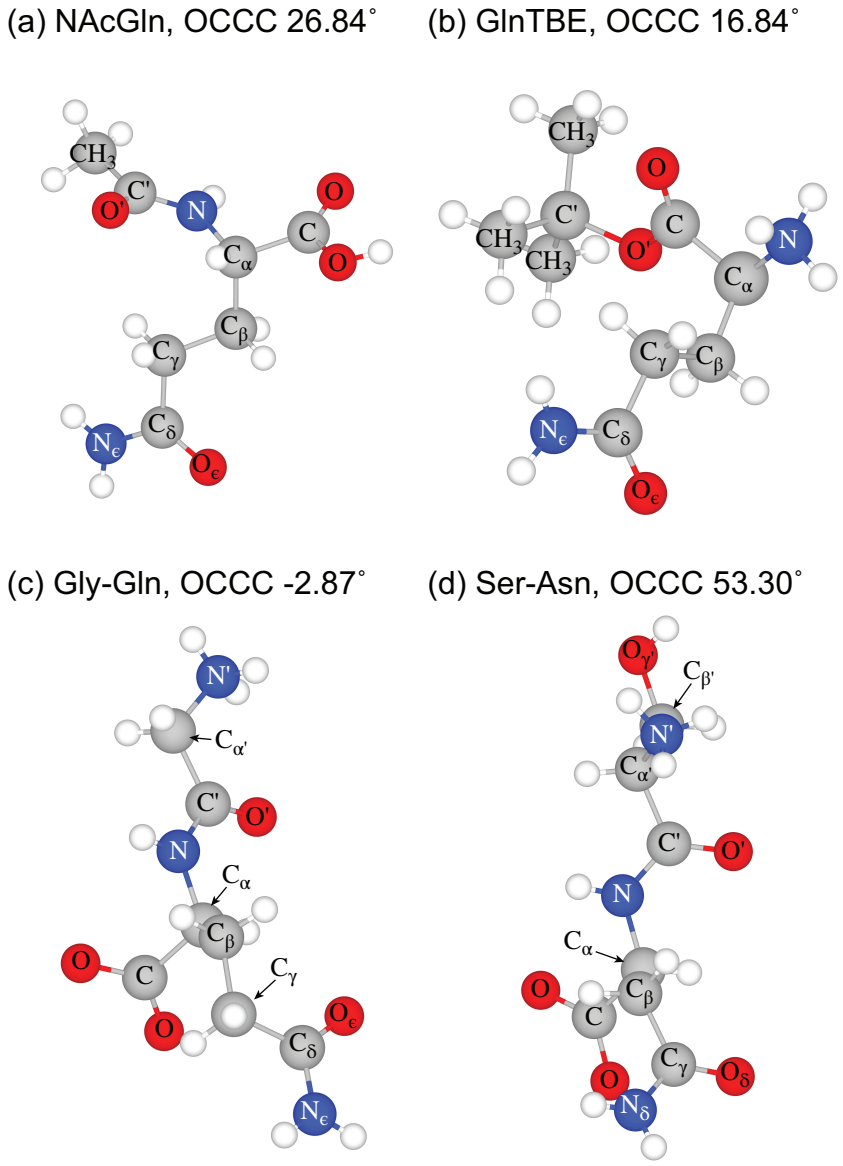

Figure 12: L-glutamine derivative molecules (a) N-Acetyl-L-glutamine, (b) L-glutamine t-butyl ester hydrochloride, (c) Glycyl-L-glutamine, and (d) L-seryl-L-asparagine with labeling scheme used in potential energy distributions and OCCC dihedral angle. Adapted with permission from [72]. Copyright © 2015, American Chemical Society.

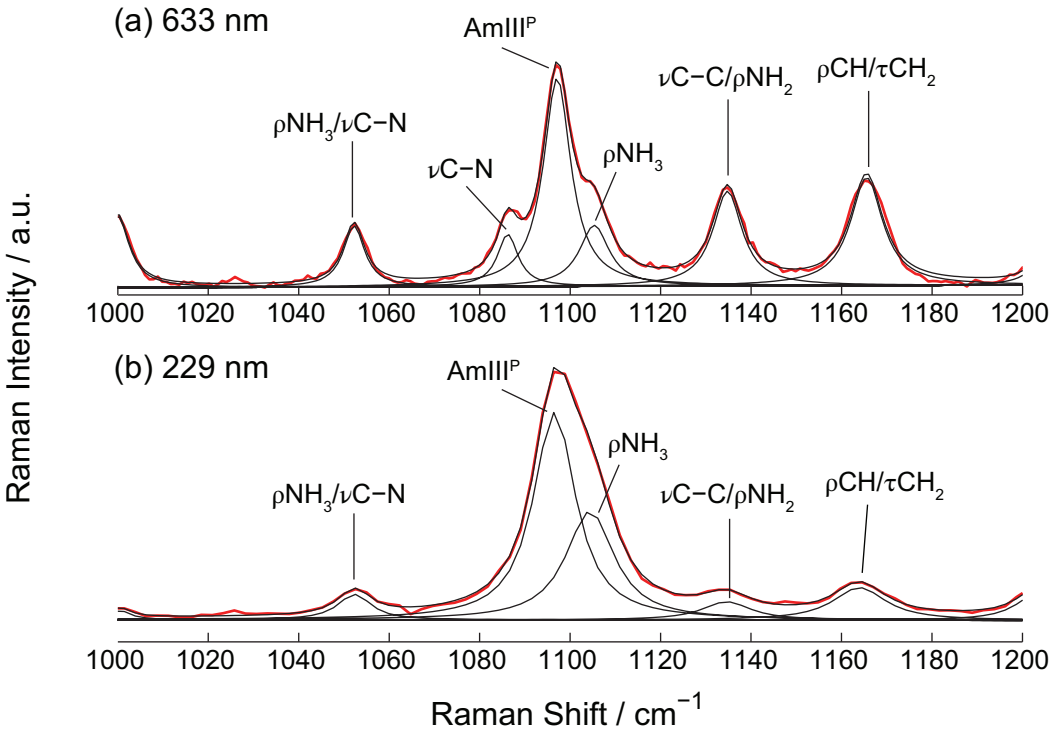

Figure 13: (a) visible Raman, and (b) UVRR spectra of crystalline L-glutamine in the 1000–1200 cm^{-1} region. Adapted with permission from [72]. Copyright © 2015, American Chemical Society.

Table 3: Raman Frequencies and Assignments of Crystalline L-Gln

Expt.[a]	Calc.	PED[b] (≥5% contribution)	Assignment
1205	1215	$-\tau C_\beta H_2$ (21), $-\nu C_\alpha C_\beta$ (18), $-\tau C_\gamma H_2$ (16), $-\rho' NH_3$ (13), $\delta NC_\alpha C(OO)$ (5)	$\tau CH_2/\nu C$–C
1166	1153	$-\rho' C_\alpha H$ (20), $\tau C_\gamma H_2$ (17), $-\rho' NH_3$ (13), $\tau C_\beta H_2$ (12), $-\nu C_\alpha C_\beta$ (8), $\rho C_\gamma H_2$ (6)	$\rho CH/\tau CH_2$
1135	1122	$\nu C_\beta C_\gamma$ (34), $\rho N_\epsilon H_2$ (17), $-\nu C_\alpha C_\beta$ (7), $\nu C_\alpha N$ (6), $-\beta N_\epsilon C_\delta C_\gamma$ (5)	νC–C/ρNH_2
1105	1109	ρNH_3 (27), $-\rho' C_\alpha H$ (10), $-\rho N_\epsilon H_2$ (10), $-\delta' NC_\alpha C(OO)$ (9), $-\rho C_\alpha H$ (7), $\nu C_\alpha N$ (7)	ρNH_3
1097	1097	$\nu C_\beta C_\gamma$ (26), $-\rho N_\epsilon H_2$ (26), $-\nu C_\delta N_\epsilon$ (13), $-\rho NH_3$ (8)	$AmIII^P$
1086	1038	$\nu C_\alpha N$ (36), $-\nu C_\beta C_\gamma$ (9), $\rho C_\beta H_2$ (8), $\rho' NH_3$ (6), $\rho C_\gamma H_2$ (5), $\rho' C_\alpha H$ (5)	νC–N
1052	1003	ρNH_3 (25), $-\nu C_\alpha N$ (19), $\rho C_\gamma H_2$ (14), $\rho C_\beta H_2$ (14), $\nu C_\alpha C_\beta$ (7), $-\tau C_\beta H_2$ (5)	$\rho NH_3/\nu$C–N
1000	974	$-\rho' NH_3$ (38), $\nu C_\alpha C_\beta$ (25), $-\nu C_\alpha C$ (8), $-\sigma CC_\alpha C_\beta$ (7), $\nu C_\alpha N$ (6)	$\rho NH_3/\nu$C–C

[a]Frequencies correspond to visible Raman (633 nm excitation) spectrum.

[b]ν: stretch; δ_s: symmetric deformation; δ: deformation; σ: scissoring; ρ: rocking; ω: wagging; β: in-plane bending; τ: twisting.

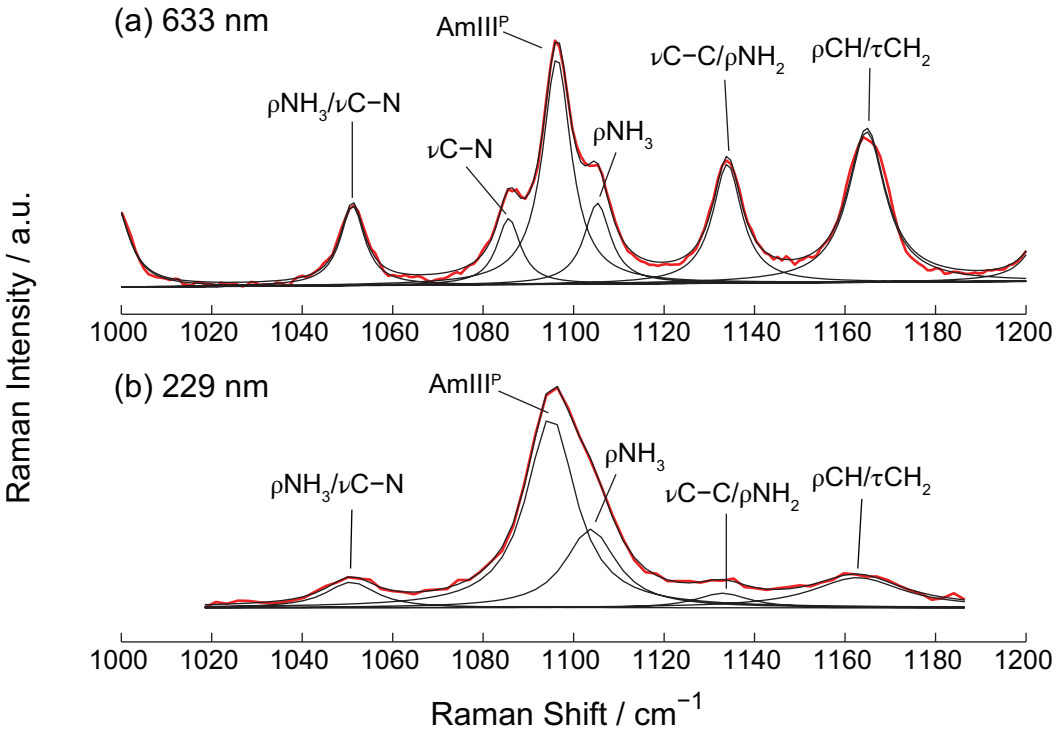

Figure 14: (a) visible Raman, and (b) UVRR spectra of crystalline D-glutamine in the 1000–1200 cm^{-1} region. Adapted with permission from [72]. Copyright © 2015, American Chemical Society.

Table 4: Raman Frequencies and Assignments of Crystalline D-Gln

Expt.[a]	Calc.	PED[b] (≥5% contribution)	Assignment
1204	1215	$-\tau C_\beta H_2$ (21), $-\nu C_\alpha C_\beta$ (18), $-\tau C_\gamma H_2$ (16), $-\rho' NH_3$ (13), $\delta NC_\alpha C(OO)$ (5)	$\tau CH_2/\nu C$–C
1165	1153	$-\rho' C_\alpha H$ (20), $\tau C_\gamma H_2$ (17), $-\rho' NH_3$ (13), $\tau C_\beta H_2$ (12), $-\nu C_\alpha C_\beta$ (8), $\rho C_\gamma H_2$ (6)	$\rho CH/\tau CH_2$
1134	1122	$\nu C_\beta C_\gamma$ (34), $\rho N_\epsilon H_2$ (17), $-\nu C_\alpha C_\beta$ (7), $\nu C_\alpha N$ (6), $-\beta N_\epsilon C_\delta C_\gamma$ (5)	νC–C/ρNH_2
1105	1109	ρNH_3 (27), $-\rho' C_\alpha H$ (10), $-\rho N_\epsilon H_2$ (10), $-\delta' NC_\alpha C(OO)$ (9), $-\rho C_\alpha H$ (7), $\nu C_\alpha N$ (7)	ρNH_3
1096	1097	$\nu C_\beta C_\gamma$ (26), $-\rho N_\epsilon H_2$ (26), $-\nu C_\delta N_\epsilon$ (13), $-\rho NH_3$ (8)	AmIII[P]
1086	1038	$\nu C_\alpha N$ (36), $-\nu C_\beta C_\gamma$ (9), $\rho C_\beta H_2$ (8), $\rho' NH_3$ (6), $\rho C_\gamma H_2$ (5), $\rho' C_\alpha H$ (5)	νC–N
1051	1003	ρNH_3 (25), $-\nu C_\alpha N$ (19), $\rho C_\gamma H_2$ (14), $\rho C_\beta H_2$ (14), $\nu C_\alpha C_\beta$ (7), $-\tau C_\beta H_2$ (5)	$\rho NH_3/\nu$C–N
999	974	$-\rho' NH_3$ (38), $\nu C_\alpha C_\beta$ (25), $-\nu C_\alpha C$ (8), $-\sigma CC_\alpha C_\beta$ (7), $\nu C_\alpha N$ (6)	$\rho NH_3/\nu$C–C

[a]Frequencies correspond to visible Raman (633 nm excitation) spectrum.
[b]ν: stretch; δ_s: symmetric deformation; δ: deformation; σ: scissoring; ρ: rocking; ω: wagging; β: in-plane bending; τ: twisting.

N-Acetyl-L-glutamine. Table 5 shows the experimentally observed Raman frequencies and assignments of crystalline NAcGln. The band at ∼1180 cm^{-1} is assigned to C_α–N stretching. This is based on the assignment of N-Acetyl-L-glutamic acid by Kausar et al. [75], who assign a similar band to nearly the same frequency. The band at ∼1138 cm^{-1} is assigned to C_α–C_β stretching/C_α–N stretching. There is no band near ∼1111 cm^{-1} in the spectrum of N-Acetyl-L-glutamic acid [75], so this band is assigned to the $N_\epsilon H_2$ rocking/C_α–C_β stretching mode. The AmIII[P] vibration is assigned to the shoulder at ∼1071 cm^{-1}. The ∼1061 cm^{-1}, ∼1022 cm^{-1}, and ∼997 cm^{-1} bands are assigned to CH_3 rocking, $C_\beta H_2$ rocking/C–H rocking, and C–CH_3 rocking of the acetyl group, respectively, as they do not exhibit pronounced shifts upon N-deuteration.

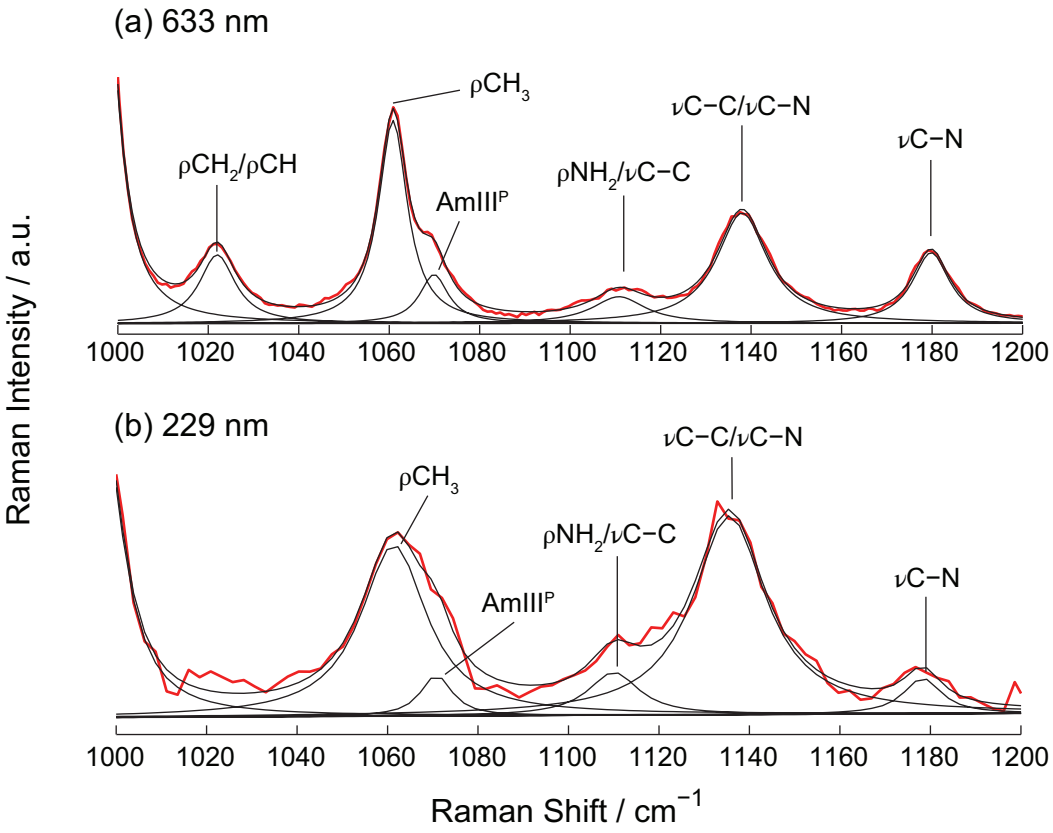

Figure 15: (a) visible Raman, and (b) UVRR spectra of crystalline N-Acetyl-L-glutamine in the 1000–1200 cm^{-1} region. Adapted with permission from [72]. Copyright © 2015, American Chemical Society.

Table 5: Raman Frequencies and Assignments of Crystalline N-Acetyl-L-Gln

Expt.[a]	Calc.	PED[b] (≥5% contribution)	Assignment
	1192	$-\tau C_\beta H_2$ (32), $-\tau C_\gamma H_2$ (24), $-\nu C_\alpha C_\beta$ (12), $\rho' C_\alpha H$ (11)	τCH_2
1180	1166	$\nu C_\alpha N$ (46), $-\delta NC_\alpha C_\beta COO$ (8), $\omega C_\beta H_2$ (7), $-\sigma C_\alpha C_\beta C_\gamma$ (6), $\nu C_\beta C_\gamma$ (5)	νC–N
1138	1119	$\nu C_\alpha C_\beta$ (22), $-\nu C_\alpha N$ (12), $\nu C_\beta C_\gamma$ (10), $\rho N_\epsilon H_2$ (8), $-\tau C_\gamma H_2$ (5)	νC–C/νC–N
1111	1110	$\rho N_\epsilon H_2$ (20), $-\nu C_\alpha C_\beta$ (15), $\nu C_\beta C_\gamma$ (14), $\rho C_\beta H_2$ (7), $\rho C_\gamma H_2$ (6), $\nu C_\delta N_\epsilon$ (5), $-\omega C_\gamma H_2$ (5)	ρNH_2/νC–C
1071	1093	$-\nu C_\beta C_\gamma$ (42), $\rho N_\epsilon H_2$ (24), $\nu C_\delta N_\epsilon$ (13)	AmIII[P]
1061	1058	ρCH_3 (63), $-\delta_s NC'O'CH_3$ (19), $-\delta_{as} CH_3$ (9), $-\rho' CH_3$ (7)	ρCH_3
1022	1043	$\rho C_\beta H_2$ (25), $\rho' C_\alpha H$ (15), $\rho C_\gamma H_2$ (14), $-\nu C_\alpha C$ (8), $\nu C_\alpha C_\beta$ (8), $\delta CC_\alpha C_\beta$ (5)	ρCH_2/ρCH
	1013	$\rho' CH_3$ (58), $-\nu C'CH_3$ (12), ρCH_3 (5), $-\delta_{as}' CH_3$ (5)	ρCH_3
997	971	$\nu C'CH_3$ (28), $\nu C'N$ (16), $\rho C'O$ (11), $-\nu C_\alpha C_\beta$ (10), $-\beta C_\alpha NC'$ (8)	νC–CH_3/νC–N

[a]Frequencies correspond to visible Raman (633 nm excitation) spectrum.
[b]ν: stretch; δ_s: symmetric deformation; δ_{as}: asymmetric deformation; δ: deformation; σ: scissoring; ρ: rocking; ω: wagging; β: in-plane bending; τ: twisting.

L-glutamine t-butyl ester hydrochloride. The Raman vibrational frequencies and assignments of crystalline GlnTBE are shown in Table 6. The band located at ∼1195 cm^{-1} is assigned to a mostly C–O stretching/CH_3 rocking vibration of the butyl ester group. Many of the bands in the spectrum of GlnTBE (Figure 16) shift in the N-deuterated spectra (not shown). Those that do not are assigned to modes that do not contain significant motion of the primary amide $N_\epsilon H_2$. These are the bands at ∼1043 cm^{-1} and ∼1030 cm^{-1}, which are assigned to C_α–N stretching/CH_3 rocking and CH_3 rocking modes, respectively. The ∼1151 cm^{-1} band is assigned to C_α–H rocking/NH_3 rocking. The NH_3 rocking/C_β–C_γ and NH_3 rocking/$N_\epsilon H_2$ rocking modes are assigned to the bands at ∼1117 cm^{-1} and ∼1105 cm^{-1} because they shift in the N-deuterated spectra. The ∼1082 cm^{-1} band shifts upon N-deuteration and is assigned to the AmIII[P] vibration. The band at ∼998 cm^{-1} is

assigned to a mostly NH_3 rocking/C_α–C_β stretching mode.

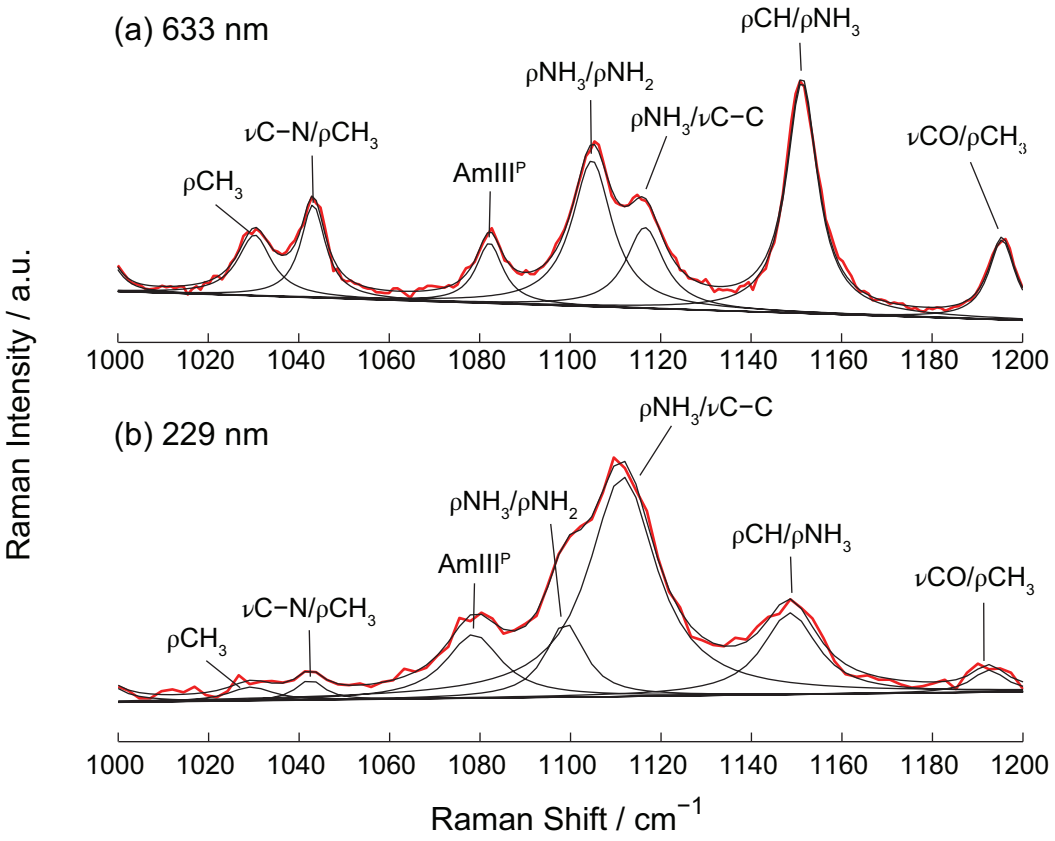

Figure 16: (a) visible Raman, and (b) UVRR spectra of crystalline L-glutamine t-butyl ester hydrochloride in the 1000–1200 cm^{-1} region. Adapted with permission from [72]. Copyright © 2015, American Chemical Society.

Table 6: Raman Frequencies and Assignments of Crystalline L-Gln t-butyl ester HCl

Expt.[a]	Calc.	PED[b] (≥5% contribution)	Assignment
1195	1195	νCO (17), ρCH_3 (10), $-\rho CH_3$ (10), $-\rho CH_3$ (9), $-\nu$CO (6), $-\delta$C'O'CCC (6), δ''C'O'CCC (6), $-\delta$'C'O'CCC (6), ρCH_3 (5), ρCH_3 (5)	$\nu CO/\rho CH_3$
1151	1161	$\rho C_\alpha H$ (23), ρNH_3 (19), $\tau C_\gamma H_2$ (11), $-\nu C_\alpha C_\beta$ (10), $\tau C_\beta H_2$ (8)	$\rho CH/\rho NH_3$
1117	1126	$-\rho NH_3$ (19), $-\nu C_\beta C_\gamma$ (16), $-\nu C_\alpha N$ (14), $\delta NC_\alpha C_\beta C$ (9), $-\rho N_\epsilon H_2$ (5)	$\rho NH_3/\nu$C–C
1105	1119	$-\rho NH_3$ (15), $\rho N_\epsilon H_2$ (14), $\rho C_\beta H_2$ (10), $\nu C_\beta C_\gamma$ (9), $\rho C_\gamma H_2$ (7), $\rho C_\alpha H$ (6), $\delta NC_\alpha C_\beta C$ (6)	$\rho NH_3/\rho NH_2$
1082	1100	$\rho N_\epsilon H_2$ (34), $-\nu C_\beta C_\gamma$ (24), $\nu C_\delta N_\epsilon$ (14), $\nu C_\delta O_\epsilon$ (5)	$AmIII^P$
1043	1068	$-\nu C_\alpha N$ (17), ρCH_3 (13), $-\rho CH_3$ (11), $-\rho CH_3$ (11), $\nu C_\beta C_\gamma$ (10), ρCH_3 (5), $\nu C_\alpha C$ (5)	νC–N/ρCH_3
1030	1058	ρCH_3 (27), $-\rho CH_3$ (26), $-\rho CH_3$ (10), ρCH_3 (10), $-\nu CCH_3$ (6)	ρCH_3
	1057	$-\nu C_\alpha N$ (24), $\nu C_\beta C_\gamma$ (11), ρCH_3 (9), ρCH_3 (8), $-\rho CH_3$ (7), $-\rho$'CH_3 (5)	νC–N/νC–C
	1014	$-\rho NH_3$ (24), $-\rho C_\beta H_2$ (18), $-\rho C_\gamma H_2$ (16), $\nu C_\alpha N$ (14), $-\nu C_\alpha C_\beta$ (5), $\tau C_\beta H_2$ (5), $-\delta_s N_\epsilon C_\delta(O_\epsilon)C_\gamma$ (5)	$\rho NH_3/\rho CH_2$
998	989	ρNH_3 (35), $\nu C_\alpha C_\beta$ (25), $-\nu C_\alpha C$ (11)	$\rho NH_3/\nu$C–C

[a]Frequencies correspond to visible Raman (633 nm excitation) spectrum.
[b]ν: stretch; δ_s: symmetric deformation; δ: deformation; σ: scissoring; ρ: rocking; ω: wagging; β: in-plane bending; τ: twisting.

Glycyl-L-glutamine. Table 7 displays the band assignments of crystalline Gly-Gln. The bands at ∼1171 cm^{-1} and ∼1139 cm^{-1} are assigned to the mostly C_α–N stretching and C_α–C_β stretching modes, respectively. The first NH_3 rocking mode is assigned to the band at ∼1124 cm^{-1}. The band located at ∼1093 cm^{-1} is assigned to the $AmIII^P$ vibration due to its sensitivity to N-deuteration. The ∼1027 cm^{-1} is assigned to $C_\beta H_2$ rocking. The remaining bands are assigned to vibrational modes that do not significantly involved the primary amide group and are shown in Table 7.

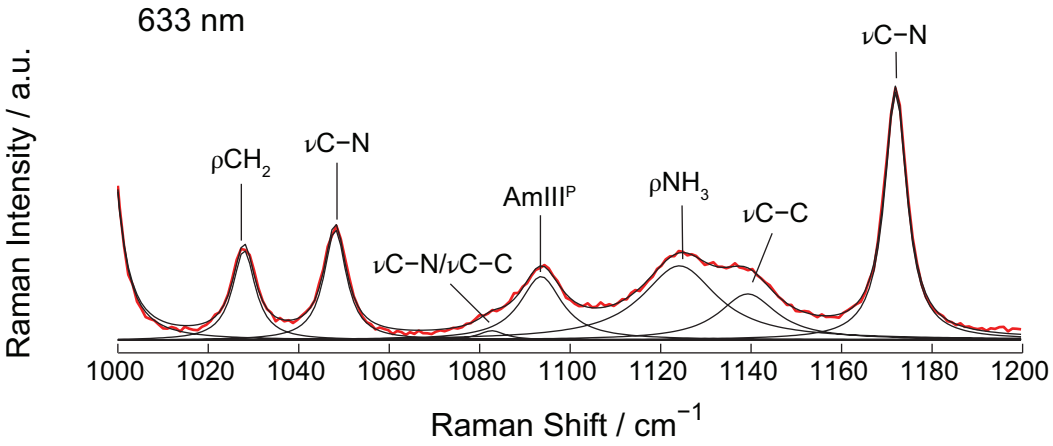

Figure 17: Visible Raman spectrum of crystalline Glycyl-L-glutamine in the 1000–1200 cm^{-1} region. Adapted with permission from [72]. Copyright © 2015, American Chemical Society.

Table 7: Raman Frequencies and Assignments of Crystalline Gly-Gln

Expt.[a]	Calc.	PED[b] (≥5% contribution)	Assignment
	1201	τ'$C_\beta H_2$ (33), $-\rho$'C_αH (24), τ'$C_\gamma H_2$ (15), $\tau C_\gamma H_2$ (6), $\nu C_\alpha C_\beta$ (5)	$\tau CH_2/\rho CH$
1171	1147	$-\nu C_\alpha$N (37), $\delta NC_\alpha C$ (7), $-\rho$N'H_3 (7), $-\nu C_{\alpha'}$N' (7)	νC–N
1139	1138	$\nu C_\alpha C_\beta$ (26), $-\nu C_\beta C_\gamma$ (19), $-\rho C_\beta H_2$ (8), $-\rho N_\epsilon H_2$ (6), $-\delta C_\alpha C_\beta C$ (6), $-\nu C_\alpha$N (6), $-\omega C_\beta H_2$ (5)	νC–C
1124	1128	ρ'N'H_3 (47), τ'$C_{\alpha'}H_2$ (18), $-\rho C_{\alpha'}H_2$ (13), $-\delta_s$C'NC_αC(OO) (5)	ρNH_3
	1105	ρN'H_3 (29), $\rho N_\epsilon H_2$ (12), $-\tau C_{\alpha'}H_2$ (7), $-\tau$'$C_{\alpha'}H_2$ (6), $\nu C_{\alpha'}$N' (6), $-\sigma$N'$C_{\alpha'}$C' (5), $-\nu C_\alpha$N (5)	ρNH_3
1093	1100	$\rho N_\epsilon H_2$ (33), $\nu C_\delta N_\epsilon$ (13), $-\rho$N'H_3 (12), $-\nu C_\beta C_\gamma$ (6), $\nu C_\delta O_\epsilon$ (5)	AmIII[P]
1082	1081	$-\nu C_{\alpha'}$N' (14), $\nu C_\beta C_\gamma$ (13), νC'$C_{\alpha'}$ (8), $\rho C_\gamma H_2$ (7), $\nu C_\alpha C_\beta$ (7), ρ'C_αH (6), $-\nu C_\alpha$N (5)	νC–N/νC–C
1048	1045	$-\nu C_{\alpha'}$N' (56), νC_αN (9), $-\nu C_\alpha C_\beta$ (7), $-\nu C_\beta C_\gamma$ (5)	νC–N
1027	1013	$\rho C_\beta H_2$ (28), $\delta C_\alpha C_\beta C$ (9), $\tau C_\gamma H_2$ (8), $-\nu C_\beta C_\gamma$ (7), $\rho C_\gamma H_2$ (5), δNC_αC' (5)	ρCH_2
997	946	νC'$C_{\alpha'}$ (19), $-\rho C_\gamma H_2$ (10), ρC'O' (9), $-\beta$NC'C_α (6), $-\beta$C'$C_{\alpha'}$N (6), $-\rho$N'H_3 (5)	νC–C/ρCH_2

[a]Frequencies correspond to visible Raman (633 nm excitation) spectrum.
[b]ν: stretch; δ_s: symmetric deformation; δ: deformation; σ: scissoring; ρ: rocking; ω: wagging; β: in-plane bending; τ: twisting.

L-seryl-L-asparagine. Vibrational frequencies and assignments of crystalline Ser-Asn are shown in Table 8. The ∼1188 cm^{-1} band is assigned to a mostly $C_{\beta'}H_2$ rocking/NH_3 rocking mode and the band at ∼1159 cm^{-1} is assigned to C_α–N stretching. The ∼1121 cm^{-1} and ∼1108 cm^{-1} bands are modes that involve the serine side chain, $C_{\beta'}$–$O_{\gamma'}$H stretching/$N_\delta H_2$ rocking and $C_{\beta'}$–$O_{\gamma'}$H stretching, respectively. The ∼1051 cm^{-1} band is assigned to the AmIII[P] vibration due to its shift upon N-deuteration. The remaining peaks are assigned to several mostly NH_3, NH_2, and CH_2 rocking modes as shown in Table 8.

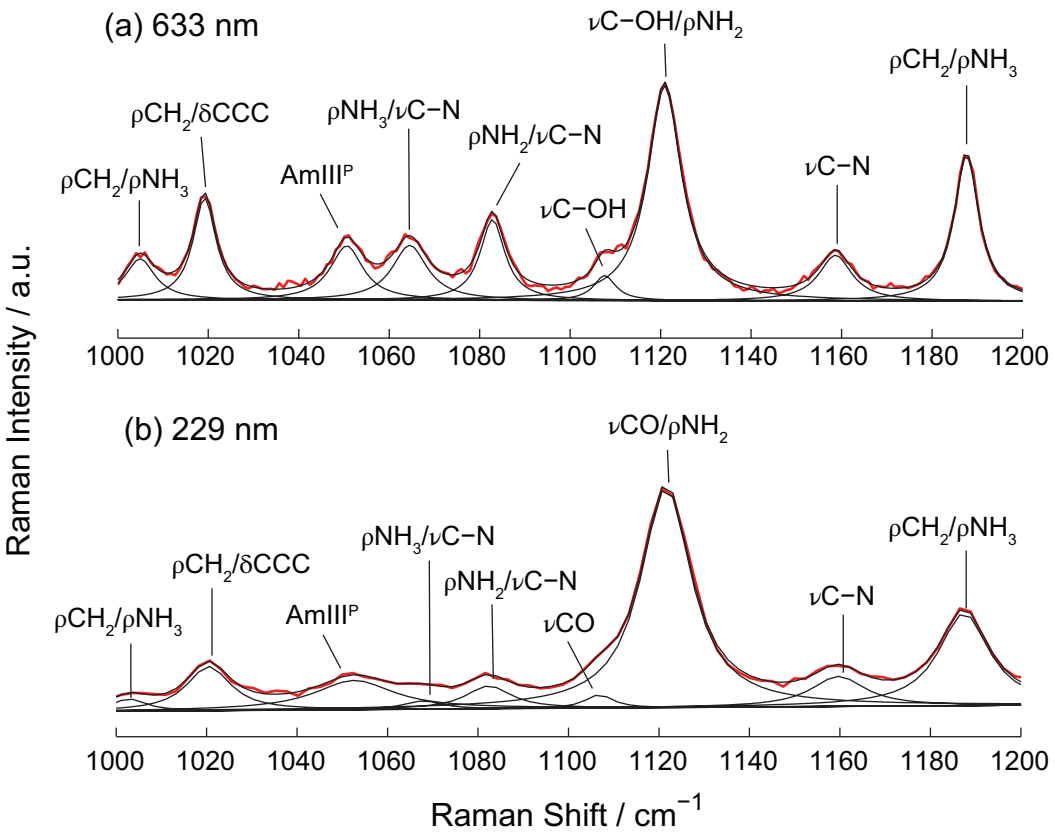

Figure 18: (a) visible Raman, and (b) UVRR spectra of crystalline L-seryl-L-asparagine in the 1000–1200 cm^{-1} region. Adapted with permission from [72]. Copyright © 2015, American Chemical Society.

Table 8: Raman Frequencies and Assignments of Crystalline Ser-Asn

Expt.[a]	Calc.	PED[b] (≥5% contribution)	Assignment
1188	1184	$-\rho C_{\beta'}H_2$ (26), $\rho'N'H_3$ (14), $-\delta NC_{\alpha'}C'$ (9), $-\tau C_{\beta'}H_2$ (8), $\beta C_{\beta'}O_{\gamma'}H$ (7), $\rho'C_{\alpha'}H$ (6), $\nu C_{\alpha'}N'$ (5), $\rho N'H_3$ (5)	$\rho CH_2/\rho NH_3$
1159	1164	$-\nu C_\alpha N$ (37), $\rho'N'H_3$ (7), $\nu C_\alpha C_\beta$ (7), $\delta CC_\alpha N$ (5), $\rho'C_\alpha H$ (5)	νC–N
1121	1119	$-\nu C_{\beta'}O_{\gamma'}H$ (17), $\rho N_\delta H_2$ (13), $\nu C_\alpha C_\beta$ (13), $\nu C_{\alpha'}N'$ (8), $-\rho'C_{\alpha'}H$ (6), $\rho N'H_3$ (5), $-\rho'N'H_3$ (5)	νC–OH/ρNH_2
1108	1116	$\nu C_{\beta'}O_{\gamma'}H$ (66), $\rho N_\delta H_2$ (9)	νC–OH
1083	1107	$-\rho N_\delta H_2$ (16), $\nu C_{\alpha'}N'$ (10), $-\rho'C_{\alpha'}H$ (10), $\nu C_{\beta'}O_{\gamma'}H$ (8), $\rho N'H_3$ (8), $-\nu C_\alpha N$ (6), $-\nu C_\delta N_\delta$ (5)	$\rho NH_2/\nu$C–N
1065	1083	$-\rho N'H_3$ (20), $\nu C_{\alpha'}N'$ (10), $-\nu C'C_{\alpha'}$ (9), $\nu C_\alpha C_\beta$ (8), $\rho C_{\alpha'}H$ (7), $-\nu C_\beta O_{\gamma'}H$ (5), $\rho'C_{\alpha'}H$ (5)	$\rho NH_3/\nu$C–N
1051	1069	$\nu C_\alpha C_\beta$ (23), $-\nu C_{\alpha'}N'$ (11), $\nu C_\alpha N$ (9), $-\delta CC_\alpha N$ (7), $-\sigma C_\alpha C_\beta C_\gamma$ (5), $-\rho N_\delta H_2$ (5)	AmIII[P]
1019	1023	$-\rho C_\beta H_2$ (23), $\delta C_\beta C_\alpha C$ (12), $\delta C'C_\alpha N$ (8), $-\nu C_\alpha C$ (7), $\delta_s C_\alpha COO$ (6), $\beta C_\alpha NC'$ (6), $\rho'C_\alpha H$ (5)	$\rho CH_2/\delta$CCC
1004	981	$\rho C_{\beta'}H_2$ (28), $\rho'N'H_3$ (25), $-\nu C_{\alpha'}C_{\beta'}$ (14), $\rho N'H_3$ (10)	$\rho CH_2/\rho NH_3$

[a]Frequencies correspond to visible Raman (633 nm excitation) spectrum.
[b]ν: stretch; δ_s: symmetric deformation; δ: deformation; σ: scissoring; ρ: rocking; ω: wagging; β: in-plane bending; τ: twisting.

Glutamine in Aqueous Solution. Previously, Ramirez and coworkers [73] assigned L-Gln in solution based on isotopic shifts and DFT calculations. Figure 19 shows the UVRR spectra of L-Gln in H_2O and D_2O. The vibrational frequencies Ramirez and coworkers report [73] do not match those reported here, and their assignments do not agree with the resonance enhancement seen in Figure 19. Thus, new assignments of L-Gln in solution were made based on more modern DFT calculations using the UVRR spectral frequencies, and previous assignment of propanamide [58]. The experimental UVRR Raman frequencies, DFT calculated frequencies, and assignments of L-Gln in H_2O in the 950–1200 cm^{-1} region can be found in Table 9.

There are several shifts in the vibrational frequencies of these bands compared to the crystal spectra, as detailed in [72]. Most notably, in the 950–1200 cm^{-1} region, the $AmIII^{P}$ vibration upshifts from ∼1097 cm^{-1} in the solid-state to ∼1110 cm^{-1} in H_2O.

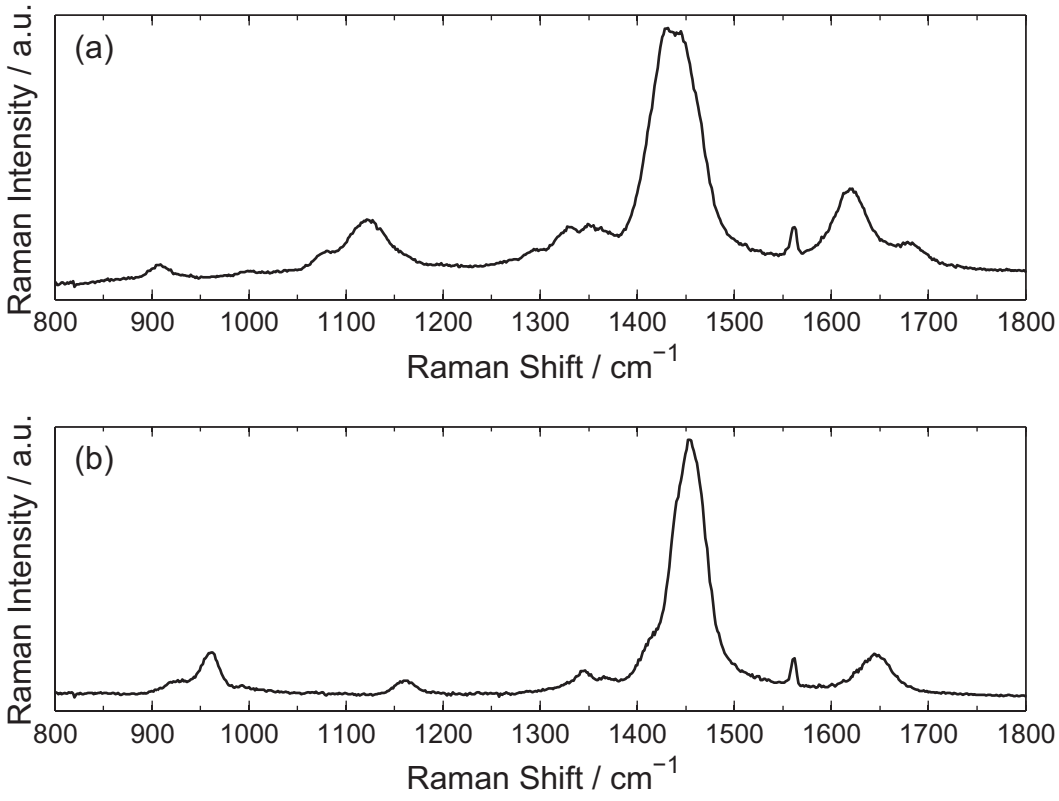

Figure 19: UVRR spectra of L-glutamine in (a) H_2O and (b) D_2O.

Table 9: UVRR Frequencies and Assignments of L-Gln in Water

Expt.	Calc.	Potential Energy Distribution[a] (≥5% contribution)
1206	1215	$-\tau C_\beta H_2$ (21), $-\nu C_\alpha C_\beta$ (18), $-\tau C_\gamma H_2$ (16), $-\rho' NH_3$ (13), $\delta NC_\alpha C(OO)$ (5)
1158	1153	$-\rho' C_\alpha H$ (20), $\tau C_\gamma H_2$ (17), $-\rho' NH_3$ (13), $\tau C_\beta H_2$ (12), $-\nu C_\alpha C_\beta$ (8), $\rho C_\gamma H_2$ (6)
1130	1122	$\nu C_\beta C_\gamma$ (34), $\rho N_\epsilon H_2$ (17), $-\nu C_\alpha C_\beta$ (7), $\nu C_\alpha N$ (6), $-\beta N_\epsilon C_\delta C_\gamma$ (5)
	1109	ρNH_3 (27), $-\rho' C_\alpha H$ (10), $-\rho N_\epsilon H_2$ (10), $-\delta' NCC(OO)$ (9), $-\rho C_\alpha H$ (7), $\nu C_\alpha N$ (7)
1110	1097	$\nu C_\beta C_\gamma$ (26), $-\rho N_\epsilon H_2$ (26), $-\nu C_\delta N_\epsilon$ (13), $-\rho NH_3$ (8)
	1038	$\nu C_\alpha N$ (36), $-\nu C_\beta C_\gamma$ (9), $\rho C_\beta H_2$ (8), $\rho' NH_3$ (6), $\rho C_\gamma H_2$ (5), $\rho' C_\alpha H$ (5)
1078	1003	ρNH_3 (25), $-\nu C_\alpha N$ (19), $\rho C_\gamma H_2$ (14), $\rho C_\beta H_2$ (14), $\nu C_\alpha C_\beta$ (7), $-\tau C_\beta H_2$ (5)
1006	974	$-\rho' NH_3$ (38), $\nu C_\alpha C_\beta$ (25), $-\nu C_\alpha C$ (8), $-\sigma CC_\alpha C_\beta$ (7), $\nu C_\alpha N$ (6)

[a] ν: stretch; δ_{as}: asymmetric deformation; δ_s: symmetric deformation; δ: deformation; σ: scissoring; ρ: rocking; ω: wagging; β: in-plane bending; τ: twisting.

3.3.2 Dependence of Primary Amide III Band on Conformation

The experimental and theoretical $AmIII^P$ vibrational frequency exhibits a cosinusoidal dependence (Figure 20(a)) on the primary amide OCCC dihedral angle [72].

Origin of the $AmIII^P$ Vibrational Frequency and OCCC Dihedral Angle Correlation. This correlation can be understood in detail by examining the results of DFT calculations carried out on L-glutamine molecules at several fixed OCCC dihedral angles. These calculations show that the $AmIII^P$ vibrational frequency correlates well with the OCCC dihedral angle (Figure 20(a)) [72]. As discussed above in Section 3.3.1, the $AmIII^P$ vibration of L-glutamine is made up of $N_\epsilon H_2$ rocking, C_δ–N_ϵ stretching, and C_β–C_γ stretching. This band composition is subject to change, however, based on the OCCC dihedral angle. For example, at certain angles, $C_\beta H_2$ twisting can also contribute significantly and the contributions of $N_\epsilon H_2$ rocking, C_δ–N_ϵ stretching, and C_β–C_γ stretching can vary.

The C_δ–N_ϵ and C_β–C_γ bond lengths affect the stretching force constants and therefore the $AmIII^P$ vibrational normal mode and frequency. This could account for the changes in normal mode composition of the $AmIII^P$ vibration that occur as the primary amide OCCC angle is varied [72]. The DFT calculated C_δ–N_ϵ and C_β–C_γ atomic distances were plotted against the OCCC dihedral angle (Figure 20). The C_β–C_γ bond length exhibits the strongest

correlation with the AmIII^{P} vibrational frequency. As the C_β–C_γ bond length increases, the AmIII^{P} vibrational frequency decreases and as the C_β–C_γ bond length decreases, the AmIII^{P} vibrational frequency increases.

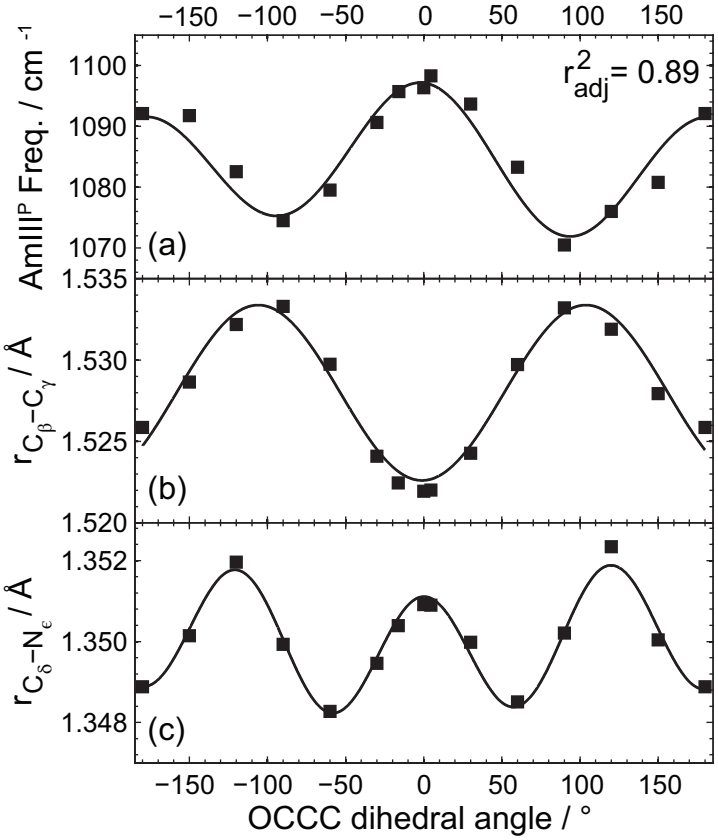

Figure 20: Calculated dependence of (a) the AmIII^{P} vibrational frequency and (b) C_β–C_γ and (c) C_δ–N bond lengths of L-glutamine on OCCC dihedral angle. Adapted with permission from [72]. Copyright © 2015, American Chemical Society.

The changes in C_β–C_γ bond length as the OCCC dihedral angle is adjusted can be explained by hyperconjugation of the C_β–C_γ σ orbital with the C_δ=O π^* orbital [72]. The C_β–C_γ bond order decreases when the σ orbital donates electron density to the π^* orbital. As the C_β–C_γ bond order decreases, the bond length increases and the stretching force constant decreases. This C_β–C_γ bond length increase downshifts the AmIII^{P} vibrational frequency.

In Figure 21, the results of the natural bond orbital (NBO) analysis are shown for L-glutamine, which estimates the electron densities of the σ and π^* orbitals. At an OCCC

dihedral angle of 0° (Figure 21(a)), the C_β–C_γ bond length is shortest and there is no hyperconjugation because of the antisymmetry of the π^* orbital. The C_β–C_γ bond length is longest when the OCCC dihedral angle is at ±90°, in Figure 21(b), where there is overlap of the C_β–C_γ σ orbital with the C_δ=O π^* orbital. At this angle the AmIII^P vibrational frequency is significantly downshifted, which suggests that the hyperconjugation of the C_β–C_γ σ orbital with the C_δ=O π^* orbital can account for the correlation of the AmIII^P vibrational frequency with the OCCC dihedral angle.

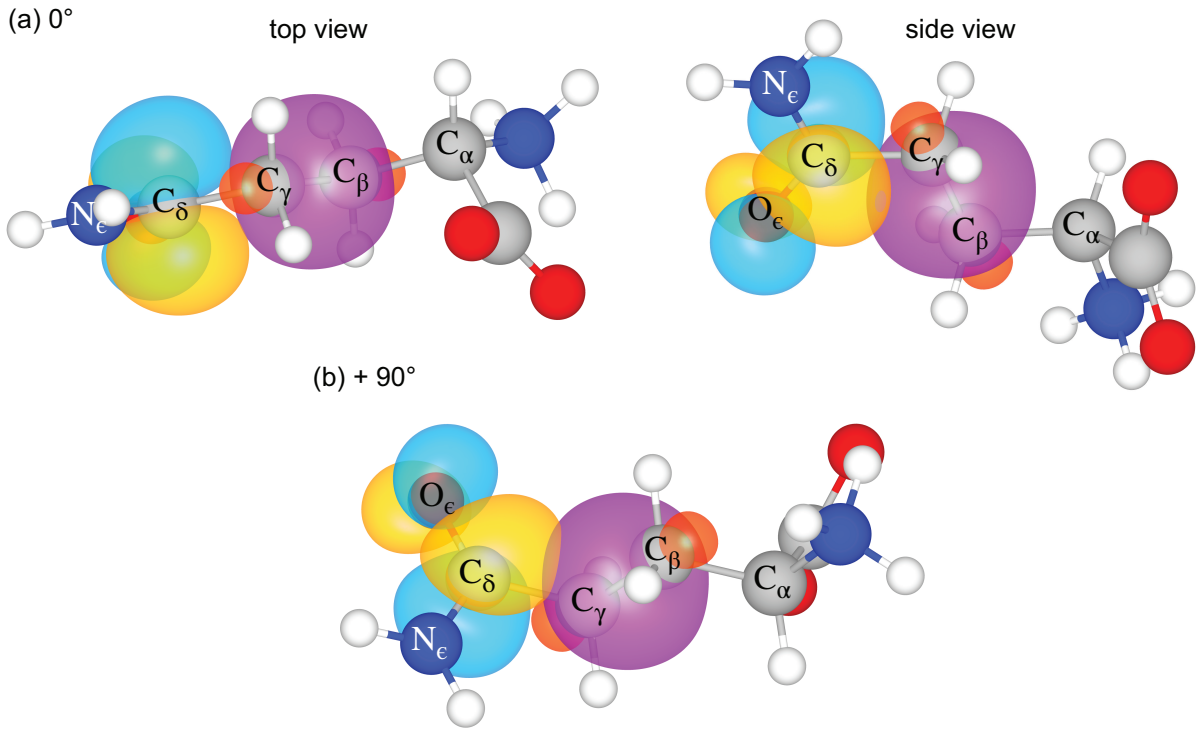

Figure 21: NBO analysis estimates C_β–C_γ σ and C_δ=O π^* molecular orbitals of L-glutamine at OCCC dihedral angles of (a) 0° and (b) ±90°. Adapted with permission from [72]. Copyright © 2015, American Chemical Society.

Experimental Correlation Between the AmIII^P Vibrational Frequency and OCCC Dihedral Angle. In Figure 22, the experimental AmIII^P vibrational frequencies from the UVRR and visible Raman spectra are plotted against the OCCC dihedral angles determined from the X-ray structures of L-glutamine and the five derivative molecules.

These data were fit with a sum of cosines:

$$\nu(\chi) = \nu_0 + A\cos(2\chi) + B\cos(\chi - C) \tag{3.1}$$

where χ is the OCCC dihedral angle, $\nu_0 = 1066$ cm^{-1}, $A = 29$ cm^{-1}, $B = 9$ cm^{-1}, and $C = 99°$ with $r^2 = 0.83$. Fitting was performed by fixing the ratio of A/B to the same value obtained by the fit to the theoretical data in Figure 20(a). The fit was obtained by performing a least-square minimization [72]. The terms with one- and two-fold symmetry in Equation 3.1 suggest steric and electronic effects, respectively [76]. Equation 3.1 is the black curve in Figure 22.

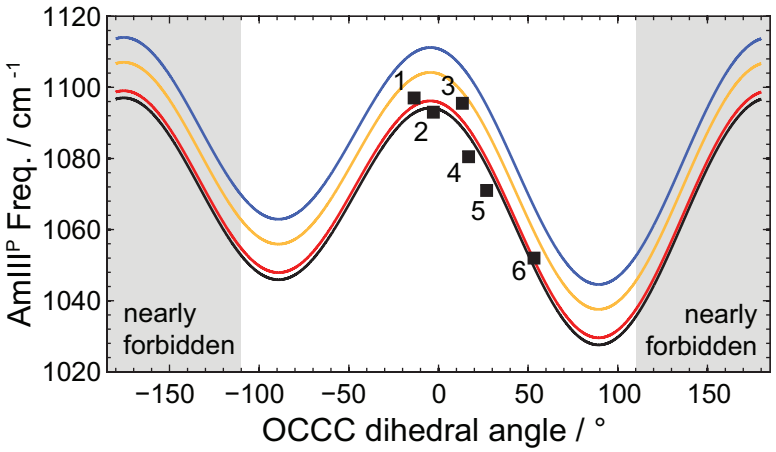

Figure 22: Experimental correlation between the AmIII^P vibrational frequency of L-glutamine and derivative molecules (1) L-Gln, (2) Gly-Gln, (3) D-Gln, (4) GlnTBE, (5) NAcGln, (6) Ser-Asn and OCCC dihedral angle. These data were fit with Equation 3.1 for four different environments of the primary amide group: crystal (black), fully hydrated (blue) low dielectric and hydrogen bonding (red), and unknown (yellow). Adapted with permission from [72]. Copyright © 2015, American Chemical Society.

The dependence of the calculated AmIII^P vibrational frequency on the primary amide OCCC dihedral angle is asymmetric about 0° (Figure 20) because of the chirality of L-glutamine. This is the reason that the AmIII^P vibrational frequency dependence on the

OCCC dihedral angle is well modeled by an expression with two cosine terms. Similar calculations were performed on the small, achiral molecule butyramide, a model of the glutamine side chain, that support this claim [72]. Butyramide does not exhibit the same asymmetry and can be represented by a simple cosine equation. D-Gln data was included in the fitting procedure described above despite the difference in chirality. This was due to the fact that the OCCC dihedral angle of D-Gln was close to 0°, mirroring L-Gln almost exactly.

As discussed in great detail in Chapter 2, the dielectric and hydrogen bonding environment can greatly influence the vibrational frequency of primary amide bands [58]. The $\mathrm{AmIII^P}$ vibrational frequency of L-glutamine shifts from 1097 $\mathrm{cm^{-1}}$ in the crystalline sample to 1110 $\mathrm{cm^{-1}}$ upon aqueous solvation. In addition, the equilibrium structure OCCC angle in solution was shown to be $\sim -12.8°$ by Rhys et al. using neutron diffraction [77]. This is very close to the $-13.54°$ of the X-ray crystal structure [78]. In order to take into account the impact of aqueous solvation on this model, the OCCC dihedral angle was set to $-13.54°$, the $\mathrm{AmIII^P}$ vibrational frequency to 1110 $\mathrm{cm^{-1}}$, and the equation was solved for ν_0. Thus, when the primary amide group is fully hydrated, $\nu_{\mathrm{hydrated}} = 1083\ \mathrm{cm^{-1}}$ in Equation 3.1 and the other parameters remain the same. This curve is shown in blue in Figure 22.

The $\mathrm{AmIII^P}$ vibrational frequency will also shift in a lower dielectric solvent, such as acetonitrile. Butyramide was used to determine the magnitude of this shift. In $\mathrm{H_2O}$, the $\mathrm{AmIII^P}$ vibrational frequency of butyramide is $\sim$1076 $\mathrm{cm^{-1}}$ and in acetonitrile it downshifts $\sim$15 $\mathrm{cm^{-1}}$ to $\sim$1064 $\mathrm{cm^{-1}}$. Parameter ν_0 in Equation 3.1 is downshifted $\sim$15 $\mathrm{cm^{-1}}$ to $\nu_{\mathrm{lowdielectric}} = 1068\ \mathrm{cm^{-1}}$ to account for this, otherwise the remaining parameters remain the same. In Figure 22, this equation is represented by the red curve.

Finally, in the case where the hydrogen bonding and dielectric environment of the primary amide group is not known, an average of the previous two situations can be used. The average of $\nu_{\mathrm{hydrated}} = 1083\ \mathrm{cm^{-1}}$ and $\nu_{\mathrm{lowdielectric}} = 1068\ \mathrm{cm^{-1}}$ is $\nu_{\mathrm{unknown}} = 1076\ \mathrm{cm^{-1}}$. Thus, Equation 3.1 with ν_{unknown}, $A = 29\ \mathrm{cm^{-1}}$, $B = 9\ \mathrm{cm^{-1}}$, and $C = 99°$ is used for unknown hydrogen bonding and dielectric environments, shown in yellow in Figure 22.

4.0 CONCLUSIONS

IR, visible Raman, and UVRR spectra of the small primary amide molecule propanamide were collected. The vibrations of propanamide were fully assigned using these data and DFT calculations. Dramatic changes in the primary amide vibrations are observed to occur upon aqueous solvation. The changes are explained in two ways: (i) an increase in molar absorptivity, due to a redshift in the NV_1 electronic transition, leads to increases in cross sections and (ii) aqueous solvation alters the dielectric and hydrogen bonding environment of the primary amide group resonance structures. This leads to a decrease in C–O and increase in C–N bond order and therefore alters the resonance enhancement and vibrational frequencies substantially. Due to this significant response, the AmI, AmII, and ν_{12} bands in particular can be used as sensitive environmental markers for the primary amide group, which is present in the protein side chains glutamine and asparagine.

Visible Raman and UVRR spectra of L-glutamine and five derivative molecules, D-glutamine, N-Acetyl-L-glutamine, L-glutamine t-butyl ester, Glycyl-L-glutamine, and L-seryl-L-asparagine were collected. Assignments were made of the vibrations of these molecules in the 950-1200 cm^{-1} region using DFT calculations. Structures of the crystalline samples were obtained by X-ray diffraction and the OCCC dihedral angles determined. A cosinusoidal dependence of the $AmIII^P$ vibrational frequency on the OCCC dihedral angle was observed. This can be explained by hyperconjugation that occurs between the C_β–C_γ σ orbital and the C_δ=O π^* orbital. When the OCCC dihedral angle is $\sim \pm 90°$, hyperconjugation results in an increase in the C_β–C_γ bong length. As the C_β–C_γ bong length increases, the stretching force constant decreases, downshifting the $AmIII^P$ band. Due to this sensitivity, the $AmIII^P$ can be used as a structural marker diagnostic of the OCCC dihedral angle in the side chains glutamine and asparagine in peptide and protein conformational studies. For

example, Punihaole et al. [72] used this relationship to determine the mean χ_3 angle of glutamines in a short polyglutamine peptide, $D_2Q_{10}K_2$, in solution to be $-32°$. This work will enable experimental measurements of glutamine and asparagine side chain conformations in samples that are insoluble and cannot be crystallized.

For example, these diagonistic primary amide bands in UVRR spectra can be used to study the environment and structure of the glutamine side chain in polyglutamine fibril-like aggregates. The dependence of primary amide bands on environment and structure can be used to test the models of polyglutamine fibril structures that were previously proposed [14–21]. UVRR could be used to confirm and gain insight into the two distinct populations of glutamine side chains observed in fibrils by ssNMR [14,19,20,22]. Recently, van der Wel and coworkers reported χ_1 ($NC_\alpha C_\beta C_\gamma$) and χ_2 ($C_\alpha C_\beta C_\gamma C_\delta$) dihedral angles of two populations of glutamine side chains in the core of huntingtin exon 1 fibrils using ssNMR [22]. Determination of the glutamine OCCC (χ_3) dihedral angle would complement these results and lead to a better understanding of the glutamine side chains in the fibril core.

Primary amide vibrations can be used to monitor the side chain glutamines and asparagines in conformational studies of peptides and proteins that have a variety of side chains. Interpretation of UVRR spectra of peptides with both backbone secondary amide and side chain primary amides is challenged by the many peaks present in this spectral region. However, this can be overcome with the use of difference spectra. Excitation at ∼200 nm selectively enhances backbone secondary amide vibrations [30]. Selective enhancement of side chain primary amide vibrations relative to backbone secondary amide vibrations can be accomplished by excitation closer to ∼190 nm [59]. By subtracting the ∼200 nm UVRR spectrum of the same sample, one can obtain a difference spectrum made up of primarily the primary amide vibrations [25]. These primary amide vibrations can be used to determine the average OCCC dihedral angle of the ensemble of glutamine or asparagine side chains present in the peptide or protein. If only one glutamine or asparagine residue is present, this allows for the determinations of the average of that residue. The understanding of the dependence of the UVRR primary amide vibrations on the structure and environmental characteristics of the primary amide group will allow for incisive studies of proteins and peptides in solution and in the solid-state.

BIBLIOGRAPHY

[1] Y. Trottier, Y. Lutz, G. Stevanin, G. Imbert, D. Devys, G. Cancel, F. Saudou, C. Weber, G. David, L. Tora, Y. Agid, A. Brice, and J. Mandel. Polyglutamine Expansion as a Pathological Epitope in Huntington's Disease and Four Dominant Cerebellar Ataxias. *Nature*, 378(6555):403–406, 1995.

[2] Christopher A. Ross and Michelle A. Poirier. Protein Aggregation and Neurodegenerative Disease. *Nature medicine*, 10:S10–S17, July 2004.

[3] Jennifer R. Gatchel and Huda Y. Zoghbi. Diseases of Unstable Repeat Expansion: Mechanisms and Common Principles. *Nature Reviews Genetics*, 6(10):743–755, October 2005.

[4] Harry T. Orr and Huda Y. Zoghbi. Trinucleotide Repeat Disorders. *Annual Review of Neuroscience*, 30:575–621, January 2007.

[5] Ronald Wetzel. Physical Chemistry of Polyglutamine: Intriguing Tales of a Monotonous Sequence. *Journal of Molecular Biology*, 421(4-5):466–90, August 2012.

[6] Regina M. Murphy, Robert H. Walters, Matthew D. Tobelmann, and Joseph P. Bernacki. When More Is Not Better: Expanded Polyglutamine Domains in Neurodegenerative Disease. In Farid Rahimi and Gal Bitan, editors, *Non-fibrillar Amyloidogenic Protein Assemblies - Common Cytotoxins Underlying Degenerative Diseases*, chapter 11, pages 337–375. Springer Netherlands, Dordrecht, 2012.

[7] Montserrat Arrasate and Steven Finkbeiner. Protein Aggregates in Huntington's Disease. *Experimental Neurology*, 238(1):1–11, November 2012.

[8] Elyse S. Blum, Andrew R. Schwendeman, and Shai Shaham. PolyQ Disease: Misfiring of a Developmental Cell Death Program? *Trends in Cell Biology*, 23(4):168–174, April 2013.

[9] Songming Chen, Frank A. Ferrone, and Ronald Wetzel. Huntington's Disease Age-of-Onset Linked to Polyglutamine Aggregation Nucleation. *Proceedings of the National Academy of Sciences of the United States of America*, 99(18):11884–11889, 2002.

[10] Anusri M. Bhattacharyya, Ashwani K. Thakur, and Ronald Wetzel. Polyglutamine Aggregation Nucleation: Thermodynamics of a Highly Unfavorable Protein Folding Reaction. *Proceedings of the National Academy of Sciences of the United States of America*, 102(43):15400–15405, October 2005.

[11] Xiaoling Wang, Andreas Vitalis, Matthew A. Wyczalkowski, and Rohit V. Pappu. Characterizing the Conformational Ensemble of Monomeric Polyglutamine. *Proteins*, 63(2):297–311, May 2006.

[12] Andreas Vitalis, Xiaoling Wang, and Rohit V. Pappu. Atomistic Simulations of the Effects of Polyglutamine Chain Length and Solvent Quality on Conformational Equilibria and Spontaneous Homodimerization. *Journal of Molecular Biology*, 384(1):279–297, December 2008.

[13] Robert H. Walters and Regina M. Murphy. Examining Polyglutamine Peptide Length: A Connection Between Collapsed Conformations and Increased Aggregation. *Journal of Molecular Biology*, 393(4):978–992, November 2009.

[14] Karunakar Kar, Cody L. Hoop, Kenneth W. Drombosky, Matthew A. Baker, Ravindra Kodali, Irene Arduini, Patrick C. A. van der Wel, W. Seth Horne, and Ronald Wetzel. β-Hairpin-Mediated Nucleation of Polyglutamine Amyloid Formation. *Journal of Molecular Biology*, 425(7):1183–1197, April 2013.

[15] M. F. Perutz, J. T. Finch, J. Berriman, and A. Lesk. Amyloid Fibers are Water-Filled Nanotubes. *Proceedings of the National Academy of Sciences of the United States of America*, 99(8):5591–5595, April 2002.

[16] Pawel Sikorski and Edward Atkins. New Model for Crystalline Polyglutamine Assemblies and Their Connection with Amyloid Fibrils. *Biomacromolecules*, 6(1):425–432, 2005.

[17] Deepak Sharma, Leonid M. Shinchuk, Hideyo Inouye, Ronald Wetzel, and Daniel A. Kirschner. Polyglutamine Homopolymers Having 8-45 Residues Form Slablike β-Crystallite Assemblies. *Proteins*, 61(2):398–411, November 2005.

[18] J. Mario Isas, Ralf Langen, and Ansgar B. Siemer. Solid-State NMR on the Static and Dynamic Domains of Huntingtin Exon-1 Fibrils. *Biochemistry*, 54(25):3942–3949, 2015.

[19] Robert Schneider, Miria C. Schumacher, Henrik Mueller, Deepak Nand, Volker Klaukien, Henrike Heise, Dietmar Riedel, Gerhard Wolf, Elmar Behrmann, Stefan Raunser, Ralf Seidel, Martin Engelhard, and Marc Baldus. Structural Characterization of Polyglutamine Fibrils by Solid-State NMR Spectroscopy. *Journal of Molecular Biology*, 412(1):121–136, September 2011.

[20] V. N. Sivanandam, Murali Jayaraman, Cody L. Hoop, Ravindra Kodali, Ronald Wetzel, and Patrick C. A. van der Wel. The Aggregation-Enhancing Huntingtin N-Terminus Is Helical in Amyloid Fibrils. *Journal of the American Chemical Society*, 133(12):4558–4566, March 2011.

[21] Cody L. Hoop, Hsiang-Kai Lin, Karunakar Kar, Zhipeng Hou, Michelle A. Poirier, Ronald Wetzel, and Patrick C. A. van der Wel. Polyglutamine Amyloid Core Boundaries and Flanking Domain Dynamics in Huntingtin Fragment Fibrils Determined by Solid-State Nuclear Magnetic Resonance. *Biochemistry*, 53(42):6653–6666, October 2014.

[22] Cody L. Hoop, Hsiang-Kai Lin, Karunakar Kar, Gábor Magyarfalvi, Jonathan M. Lamley, Jennifer C. Boatz, Abhishek Mandal, Józef R. Lewandowski, Ronald Wetzel, and Patrick C. A. van der Wel. Huntingtin Exon 1 Fibrils Feature an Interdigitated β-HairpinBased Polyglutamine Core. *Proceedings of the National Academy of Sciences*, 113(6):1546–1551, 2016.

[23] Rebecca Nelson, Michael R. Sawaya, Melinda Balbirnie, Anders Ø. Madsen, Christian Riekel, Robert Grothe, and David Eisenberg. Structure of the Cross-Beta Spine of Amyloid-like Fibrils. *Nature*, 435(7043):773–8, June 2005.

[24] Antonino Natalello, Anna Maria Frana, Annalisa Relini, Alessandra Apicella, Gaetano Invernizzi, Carlo Casari, Alessandra Gliozzi, Silvia Maria Doglia, Paolo Tortora, and Maria Elena Regonesi. A Major Role for Side-Chain Polyglutamine Hydrogen Bonding in Irreversible Ataxin-3 Aggregation. *PloS ONE*, 6(4):e18789, January 2011.

[25] Kan Xiong, David Punihaole, and Sanford A. Asher. UV Resonance Raman Spectroscopy Monitors Polyglutamine Backbone and Side Chain Hydrogen Bonding and Fibrillization. *Biochemistry*, 51(29):5822–5830, July 2012.

[26] Daniel C. Harris and Michael D. Bertolucci. *Symmetry and Spectroscopy: An Introduction to Vibrational and Electronic Spectroscopy*. Dover Publications, 1978.

[27] Derek A. Long. *The Raman Effect: A Unified Treatment of the Theory of Raman Scattering by Molecules*. John Wiley & Sons Ltd, West Sussex, England, 2002.

[28] Sanford A. Asher. Ultraviolet Raman Spectrometry. In J.M. Chalmers and P.R. Griffiths, editors, *Handbook of Vibrational Spectroscopy*, pages 557–571. John Wiley & Sons, Ltd., 2002.

[29] Sulayman A. Oladepo, Kan Xiong, Zhenmin Hong, Sanford A. Asher, Joseph Handen, and Igor K. Lednev. UV Resonance Raman Investigations of Peptide and Protein Structure and Dynamics. *Chemical Reviews*, 112(5):2604–2628, May 2012.

[30] John M. Dudik, Craig R. Johnson, and Sanford A. Asher. UV Resonance Raman Studies of Acetone, Acetamide, and N-Methylacetamide: Models for the Peptide Bond. *The Journal of Physical Chemistry*, 89(18):3805–3814, 1985.

[31] Yang Wang, Roberto Purrello, Savas Georgiou, and Thomas G. Spiro. UVRR Spectroscopy of the Peptide Bond. 2. Carbonyl H-Bond Effects on the Ground- and Excited-State Structures of N-methylacetamide. *Journal of the American Chemical Society*, 113(17):6368–6377, 1991.

[32] Nancy E. Triggs and James J. Valentini. An Investigation of Hydrogen Bonding in Amides Using Raman Spectroscopy. *The Journal of Physical Chemistry*, 6931(49):6922–6931, 1992.

[33] Laura M. Markham and Bruce S. Hudson. Ab Initio Analysis of the Effects of Aqueous Solvation on the Resonance Raman Intensities of N-Methylacetamide. *Journal of Physical Chemistry*, 100(7):2731–2737, 1996.

[34] Nataliya S. Myshakina, Zeeshan Ahmed, and Sanford A. Asher. Dependence of Amide Vibrations on Hydrogen Bonding. *The Journal of Physical Chemistry B*, 112(38):11873–11877, September 2008.

[35] Sanford A. Asher, Anatoli Ianoul, Guido Mix, Mary N. Boyden, Anton Karnoup, Max Diem, and Reinhard Schweitzer-Stenner. Dihedral Ψ Angle Dependence of the Amide III Vibration: A Uniquely Sensitive UV Resonance Raman Secondary Structural Probe. *Journal of the American Chemical Society*, 123(11):11775–11781, 2001.

[36] Sanford A. Asher, Alexander V. Mikhonin, and Sergei Bykov. UV Raman Demonstrates that α-Helical Polyalanine Peptides Melt to Polyproline II Conformations. *Journal of the American Chemical Society*, 126(21):8433–8440, 2004.

[37] Alexander V. Mikhonin, Zeeshan Ahmed, Anatoli Ianoul, and Sanford A. Asher. Assignments and Conformational Dependencies of the Amide III Peptide Backbone UV Resonance Raman Bands. *The Journal of Physical Chemistry B*, 108(49):19020–19028, December 2004.

[38] Aleksandr V. Mikhonin, Sergei V. Bykov, Nataliya S. Myshakina, and Sanford A. Asher. Peptide Secondary Structure Folding Reaction Coordinate: Correlation Between UV Raman Amide III Frequency, Ψ Ramachandran Angle, and Hydrogen Bonding. *The Journal of Physical Chemistry B*, 110(4):1928–1943, 2006.

[39] Aleksandr V. Mikhonin, Nataliya S. Myshakina, Sergei V. Bykov, and Sanford A. Asher. UV Resonance Raman Determination of Polyproline II , Extended 2.5(1)-Helix , and β-Sheet Ψ Angle Energy Landscape in Poly-L-Lysine and Poly-L-Glutamic Acid. *Journal of the American Chemical Society*, 127(26):7712–7720, 2005.

[40] Aleksandr V. Mikhonin and Sanford A. Asher. Direct UV Raman Monitoring of 310-Helix and π-Bulge Premelting During α-Helix Unfolding. *Journal of the American Chemical Society*, 128(42):13789–13795, 2006.

[41] Lu Ma, Zeeshan Ahmed, Aleksandr V. Mikhonin, and Sanford A. Asher. UV Resonance Raman Measurements of Poly-L-Lysine's Conformational Energy Landscapes: Dependence on Perchlorate Concentration and Temperature. *Journal of Physical Chemistry B*, 111(412):7675–7680, 2007.

[42] Kan Xiong, Eliana K. Asciutto, Jeffry D. Madura, and Sanford A. Asher. Salt Dependence of an α-Helical Peptide Folding Energy Landscapes. *Biochemistry*, 48(45):10818–10826, November 2009.

[43] Kan Xiong and Sanford A. Asher. Circular Dichroism and UV Resonance Raman Study of the Impact of Alcohols on the Gibbs Free Energy Landscape of an α-Helical Peptide. *Biochemistry*, 49(15):3336–3342, April 2010.

[44] Lu Ma, Zhenmin Hong, Bhavya Sharma, and Sanford Asher. UV Resonance Raman Studies of the NaClO4 Dependence of Poly-L-Lysine Conformation and Hydrogen Exchange Kinetics. *Journal of Physical Chemistry B*, 116(3):1134–1142, 2012.

[45] Zhenhuan Chi and Sanford A. Asher. UV Raman Determination of the Environment and Solvent Exposure of Tyr and Trp Residues. *The Journal of Physical Chemistry B*, 102(47):9595–9602, November 1998.

[46] Takashi Miura, Hideo Takeuchi, and Issei Harada. Tryptophan Raman Bands Sensitive to Hydrogen Bonding and Side-Chain Conformation. *Journal of Raman Spectroscopy*, 20(10):667–671, 1989.

[47] Teruhiko Maruyama and Hideo Takeuchi. Effects on Hydrogen Bonding and Side-Chain Conformation on the Raman Bands of Tryptophan-2,4,5,6,7-d5. *Journal of Raman Spectroscopy*, 26:319–324, 1995.

[48] Hideo Takeuchi. Raman Spectral Marker of Tryptophan Conformation: Theoretical Basis and Extension to a Wider Range of Torsional Angle. *Journal of Molecular Structure*, 1023:143–148, September 2012.

[49] Zhenmin Hong, Jonathan Wert, and Sanford A. Asher. UV Resonance Raman and DFT Studies of Arginine Side Chains in Peptides: Insights into Arginine Hydration. *The Journal of Physical Chemistry B*, 117(24):7145–7156, June 2013.

[50] Debra S. Caswell and Thomas G. Spiro. Ultraviolet Resonance Raman Spectroscopy of Imidazole, Histidine, and Cu(imidazole)42+: Implications for Protein Studies. *Journal of the American Chemical Society*, 6477(10):6470–6477, 1986.

[51] Laura M. Markham, Leland C. Mayne, Bruce S. Hudson, and Marek Z. Zgierski. Resonance Raman Studies of Imidazole, Imidazolium, and Their Derivatives: The Effect of Deuterium Substitution. *The Journal of Physical Chemistry*, 97(40):10319–10325, October 1993.

[52] Gregory P. Harhay and Bruce S. Hudson. Ultraviolet Resonance Raman Study of Proline Isomerization. *The Journal of Physical Chemistry*, 95(9):3511–3513, 1991.

[53] Trace Jordan, Ishita Mukerji, Yang Wang, and Thomas G. Spiro. UV Resonance Raman Spectroscopy and Hydrogen Bonding of the Proline Peptide Bond. *Journal of Molecular Structure*, 379(1):51–64, 1996.

[54] Zeeshan Ahmed, Nataliya S. Myshakina, and Sanford A. Asher. Dependence of the AmII'p Proline Raman Band on Peptide Conformation. *The Journal of Physical Chemistry B*, 113(32):11252–11259, August 2009.

[55] Melissa D. Michelitsch and Jonathan S. Weissman. A Census of Glutamine/Asparagine-Rich Regions: Implications for their Conserved Function and the Prediction of Novel Prions. *Proceedings of the National Academy of Sciences*, 97(22):11910–11915, 2000.

[56] Takehiko Shimanouchi. Tables of Molecular Vibrational Frequencies Consolidated Volume I, 1972.

[57] Sanford A. Asher, Richard W. Bormett, X. G. Chen, Donald H. Lemmon, Namjun Cho, Marco Arrigoni, Luis Spinelli, and Jeff Cannon. UV Resonance Raman Spectroscopy Using a New cw Laser Source: Convenience and Experimental Simplicity. *Applied Spectroscopy*, 47(5):628–633, 1993.

[58] David Punihaole, Ryan S. Jakubek, Elizabeth M. Dahlburg, Zhenmin Hong, Nataliya S. Myshakina, Steven Geib, and Sanford A. Asher. UV Resonance Raman Investigation of the Aqueous Solvation Dependence of Primary Amide Vibrations. *The Journal of Physical Chemistry B*, 119(10):3931–3939, 2015.

[59] Leigh B. Clark. Polarization Assignments in the Vacuum UV Spectra of the Primary Amide, Carboxyl, and Peptide Groups. *Journal of the American Chemical Society*, 117(30):7974–7986, 1995.

[60] Yoshihiro Kuroda, Yutaka Saito, Katsunosuke Machida, and Toyozo Uno. Vibrational Spectra of Propionamide and Its C– and N–Deuterated Compounds. *Bulletin of the Chemical Society of Japan*, 45:2371–2383, 1972.

[61] B. Nolin and R. Norman Jones. The Infrared Absorption Spectra of Diethyl Ketone and its Deuterium Substitution Products. *Journal of the American Chemical Society*, 75(22):5626–5628, 1953.

[62] G. Nandini and D. N. Sathyanarayana. Ab Initio Studies on Molecular Conformation and Vibrational Spectra of Propionamide. *Journal of Molecular Structure (Theochem)*, 586(1):125–135, June 2002.

[63] L. J. Bellamy. *The Infra-red Spectra of Complex Molecules*. Chapman and Hall, London, 3rd edition, 1975.

[64] Leland C. Mayne and Bruce Hudson. Resonance Raman Spectroscopy of N-Methylacetamide: Overtones and Combinations of the C–N Stretch (Amide II') and Effect of Solvation on the C=O Stretch (Amide I) Intensity. *The Journal of Physical Chemistry*, 95(8):2962–2967, 1991.

[65] Bruce S. Hudson and Laura M. Markham. Resonance Raman Spectroscopy as a Test of Ab Initio Methods for the Computation of Molecular Potential Energy Surfaces. *Journal of Raman Spectroscopy*, 29(6):489–500, 1998.

[66] E. B. Nielsen and J. A. Schellman. The Absorption Spectra of Simple Amides and Peptides. *The Journal of Physical Chemistry*, 71(7):2297–2304, June 1967.

[67] E. James Milner-White. The Partial Charge of the Nitrogen Atom in Peptide Bonds. *Protein Science*, 6(11):2477–2482, 1997.

[68] Eric J. Heller, Robert L. Sundberg, and David Tannor. Simple Aspects of Raman Scattering. *The Journal of Physical Chemistry*, 4777(2):1822–1833, 1982.

[69] Sanford A. Asher, Zhenhuan Chi, and Pusheng Li. Resonance Raman Examination of the Two Lowest Amide $\pi\pi^*$ Excited States. *Journal of Raman Spectroscopy*, 931(10-11):927–931, 1998.

[70] X. G. Chen, Sanford A. Asher, Reinhard Schweitzer-Stenner, Noemi G. Mirkin, and Samuel Krimm. UV Raman Determination of the $\pi\pi^*$ Excited State Geometry of N-Methylacetamide: Vibrational Enhancement Pattern. *Journal of the American Chemical Society*, 117(10):2884–2895, 1995.

[71] Sergei V. Bykov, Nataliya S. Myshakina, and Sanford A. Asher. Dependence of Glycine CH2 Stretching Frequencies on Conformation, Ionization State, and Hydrogen Bonding. *The Journal of Physical Chemistry B*, 112(18):5803–5812, 2008.

[72] David Punihaole, Zhenmin Hong, Ryan S. Jakubek, Elizabeth M. Dahlburg, Steven Geib, and Sanford A. Asher. Glutamine and Asparagine Side Chain Hyperconjugation-Induced Structurally Sensitive Vibrations. *The Journal of Physical Chemistry B*, 119(41):13039–13051, 2015.

[73] F. J. Ramirez, I. Tunon, and E. Silla. Amino Acid Chemistry in Solution: Structural Study and Vibrational Dynamics of Glutamine in Solution. An ab initio Reaction Field Model. *The Journal of Physical Chemistry B*, 102(32):6290–6298, 1998.

[74] P. Dhamelincourt and F. J. Ramirez. Polarized Micro-Raman and FT-IR Spectra of L-Glutamine. *Applied Spectroscopy*, 47(4):446–451, 1993.

[75] Nighat Kausar, Bruce D. Alexander, Trevor J. Dines, Robert Withnall, and Babur Z. Chowdhry. Vibrational Spectroscopy and DFT Calculations of Amino Acid Derivatives: N-Acetyl-L-Asp and N-Acetyl-L-Glu in the Solid State. *Journal of Raman Spectroscopy*, 40(6):670–678, June 2009.

[76] Norman L. Allinger, Donna Hindman, and Helmut Honig. Conformational Analysis. 125. The Importance of Twofold Barriers in Saturated Molecules. *Journal of the American Chemical Society*, 99(10):3282–3284, 1977.

[77] N. H. Rhys, A. K. Soper, and L. Dougan. The Hydrogen-Bonding Ability of the Amino Acid Glutamine Revealed by Neutron Diffraction Experiments. *The Journal of Physical Chemistry B*, 116(45):13308–13319, 2012.

[78] W. Cochran and Bruce R. Penfold. The Crystal Structure of L-Glutamine. *Acta Crystallographica*, 5(5):644–653, 1952.